Article

Cell Reports

Combined Rehabilitation Promotes the Recovery of Structural and Functional Features of Healthy Neuronal Networks after Stroke

Graphical Abstract

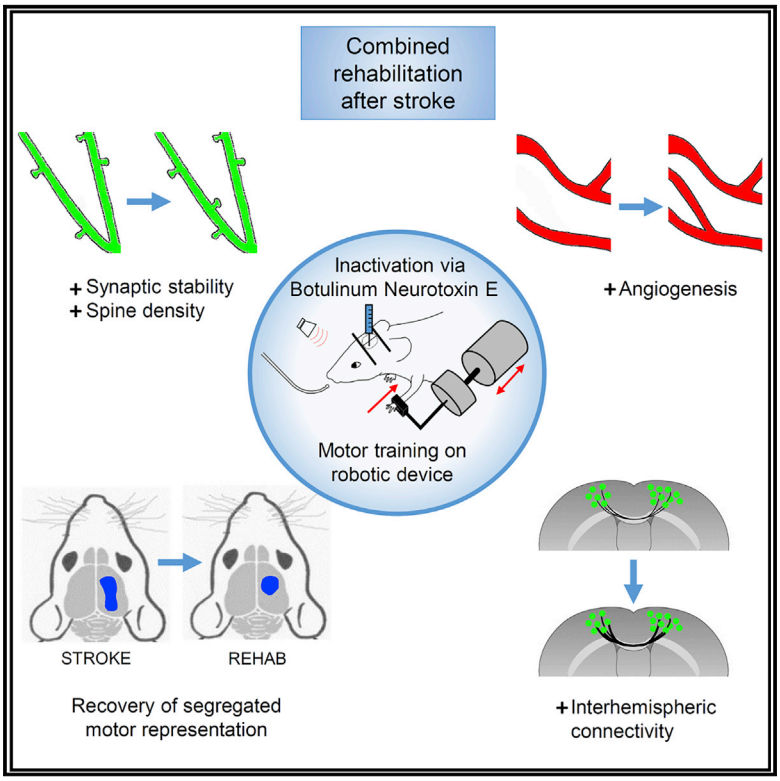

Highlights

- Post-stroke cortical plasticity is addressed by optical imaging and manipulation tools
- Combined rehabilitation stabilizes synaptic contacts in the peri-infarct area
- Increased blood vessel density is associated with perilesional angiogenesis
- Restored cortical activation has features typical of pre-stroke conditions

Authors

Anna Letizia Allegra Mascaro, Emilia Conti, Stefano Lai, ..., Silvestro Micera, Matteo Caleo, Francesco Saverio Pavone

Correspondence

allegra@lens.unifi.it

In Brief

Robotic training combined with transient contralesional inactivation was recently shown to promote a generalized recovery after stroke. Here, Allegra Mascaro et al. investigate how this rehabilitation paradigm affects neuronal and vascular plasticity of the mouse cortex. Synaptic stabilization is associated with angiogenesis and recovery of a segregated motor representation.

Allegra Mascaro et al., 2019, Cell Reports *28*, 3474–3485
September 24, 2019
https://doi.org/10.1016/j.celrep.2019.08.062

CellPress

OPEN ACCESS
CellPress

Cell Reports
Article

Combined Rehabilitation Promotes the Recovery of Structural and Functional Features of Healthy Neuronal Networks after Stroke

Anna Letizia Allegra Mascaro,[1,2,8,9,*] Emilia Conti,[2,3,9] Stefano Lai,[4] Antonino Paolo Di Giovanna,[2] Cristina Spalletti,[1] Claudia Alia,[1] Alessandro Panarese,[4] Alessandro Scaglione,[2] Leonardo Sacconi,[2,5] Silvestro Micera,[4,6] Matteo Caleo,[1,7] and Francesco Saverio Pavone[2,3,5]

[1]Neuroscience Institute, National Research Council, Pisa 56124, Italy
[2]European Laboratory for Non-Linear Spectroscopy, University of Florence, Sesto Fiorentino 50019, Italy
[3]Department of Physics and Astronomy, University of Florence, Sesto Fiorentino 50019, Italy
[4]Translational Neural Engineering Area, The BioRobotics Institute, Scuola Superiore Sant'Anna, Pisa 56127, Italy
[5]National Institute of Optics, National Research Council, Sesto Fiorentino 50019, Italy
[6]Bertarelli Foundation Chair in Translational NeuroEngineering, Centre for Neuroprosthetics and Institute of Bioengineering, École Polytechnique Fédérale de Lausanne (EPFL), Lausanne 1015, Switzerland
[7]Department of Biomedical Sciences, University of Padua, Padova 35131, Italy
[8]Lead Contact
[9]These authors contributed equally
*Correspondence: allegra@lens.unifi.it
https://doi.org/10.1016/j.celrep.2019.08.062

SUMMARY

Rehabilitation is considered the most effective treatment for promoting the recovery of motor deficits after stroke. One of the most challenging experimental goals is to unambiguously link brain rewiring to motor improvement prompted by rehabilitative therapy. Previous work showed that robotic training combined with transient inactivation of the contralesional cortex promotes a generalized recovery in a mouse model of stroke. Here, we use advanced optical imaging and manipulation tools to study cortical remodeling induced by this rehabilitation paradigm. We show that the stabilization of peri-infarct synaptic contacts accompanies increased vascular density induced by angiogenesis. Furthermore, temporal and spatial features of cortical activation recover toward pre-stroke conditions through the progressive formation of a new motor representation in the peri-infarct area. In the same animals, we observe reinforcement of inter-hemispheric connectivity. Our results provide evidence that combined rehabilitation promotes the restoration of structural and functional features distinctive of healthy neuronal networks.

INTRODUCTION

Every year, several million stroke victims worldwide are impaired by long-term disability, imparting a large societal and personal burden in terms of lost productivity, lost independence, and social withdrawal (Mozaffarian et al., 2015). When stroke affects the motor-associated cortices, the recovery of motor function is often partial, owing to the limited degree of spontaneous brain repair (Carmichael et al., 2017). Strategies that promote brain plasticity, like pharmacological treatments and physical training, can enhance neural rewiring and dramatically improve functional motor recovery. Pharmacological treatment in both the peri-infarct and contralesional areas has been shown to aid the restoration of function (e.g., see Clarkson et al., 2010). Another highly effective rehabilitative approach after stroke is physical training (Bütefisch, 2006; Jones and Adkins, 2015). The effectiveness of rehabilitative therapies can be maximized through a combination of treatments (Adkins-Muir and Jones, 2003; Dancause and Nudo, 2011; Hesse et al., 2007; Plautz et al., 2003). A few animal studies provided valuable insights into the anatomical adaptations in rodents and primates induced by coupled therapies (Fang et al., 2010; Lee et al., 2004; Plautz et al., 2003; Wahl et al., 2014). In a recent study on mice, Spalletti et al. (2017) took advantage of a rehabilitation paradigm that combines motor training and pharmacological inhibition of the contralesional primary motor cortex (M1) with botulinum neurotoxin E (BoNT/E). A BoNT/E injection reduced the excessive transcallosal inhibition exerted from the healthy to the stroke side (Spalletti et al., 2017). The combination of motor training and BoNT/E silencing was superior to either treatment alone in promoting the recovery of motor skills in stroke mice. Importantly, this combined therapy led to motor improvements that generalized to multiple motor tasks (Spalletti et al., 2017). The induction of a generalized functional gain (i.e., the recovery of motor functions beyond the ones that are trained) is crucial when evaluating the efficacy of rehabilitative therapies.

In the last decade, fluorescence imaging has provided valuable insights into spontaneous cortical plasticity after stroke. Structural plasticity after stroke has been evaluated by two-photon fluorescence (TPF) microscopy (Brown et al., 2007; Johnston et al., 2013; Mostany et al., 2010; Sakadžić et al., 2015), showing that the extent of synaptic recovery varied along the distance from the infarct core (Sigler and Murphy, 2010) and

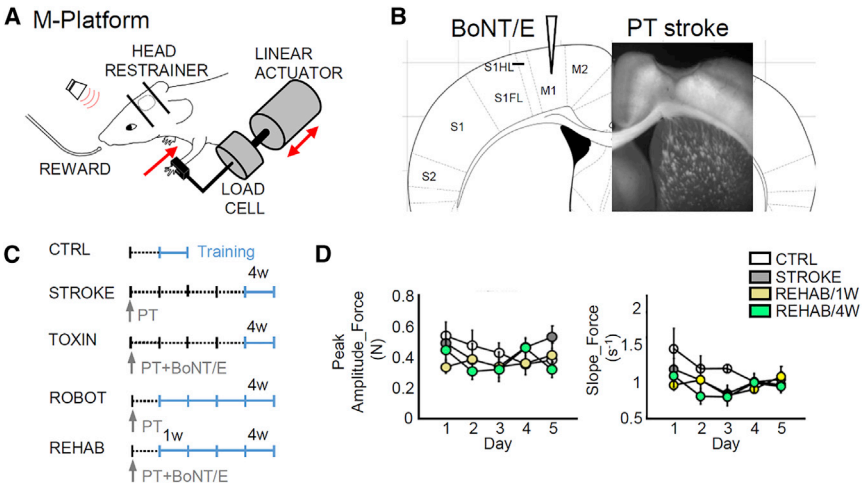

Figure 1. Experimental Design

(A) Schematic representation of the M-Platform that was used for motor training.

(B) Schematic of the experimental protocol, which combines the photothrombotic stroke in the primary motor cortex (M1) with a contralesional injection of BoNT/E into the homotopic cortex.

(C) The experimental timeline for the CTRL, STROKE, TOXIN, ROBOT, and REHAB groups in the awake imaging experiment. Light blue lines refer to training weeks. W, week; PT, photothrombosis.

(D) Graphs showing the peak amplitude (left) and slope (right) of the force signals (average ± SEM) recorded in the pulling phase during training on the M-Platform over 5 days (4 weeks after injury for STROKE mice, 1 and 4 weeks after injury for REHAB mice, and during the week of training for CTRL mice; n $mice_{CTRL}$ = 4, n $transients_{CTRL}$ = 272; n $mice_{STROKE}$ = 6, n $transients_{STROKE}$ = 308; n $mice_{REHAB}$ = 6, n $transients_{REHAB/1W}$ = 407, n $transients_{REHAB/4W}$ = 343). Values are average ± SEM. There is no significant difference among the groups over the 5 days.

See also Video S1.

that the redistribution of blood vessel and dendrite orientation was confined to the peri-infarct area (Brown et al., 2007). In parallel, Murphy and colleagues performed a number of acute optical imaging studies showing the persistence of cortical functional remapping over months after stroke (Brown et al., 2009; Harrison et al., 2013). The availability of a new generation of experimental tools, like optogenetics (Ayling et al., 2009; Lim et al., 2014) and genetically encoded functional indicators (Chen et al., 2013), provided new means of exploring neuronal rewiring.

To our knowledge, no investigation has yet described how rehabilitation after stroke affects cortical structural and functional plasticity *in vivo* and on the long-term scale. Many unanswered questions need to be addressed, like how rehabilitation molds neuronal structural plasticity and cortical functional maps. Moreover, it is still to be defined if neuronal and vascular plasticity act in concert to aid functional recovery.

In the present study, we dissected how rehabilitative treatment activates concurrent modalities of cortical plasticity in mice by using a combination of cutting-edge optical techniques. Our experiments revealed that a combination of physical training and pharmacological manipulation of the contralesional activity helps the preservation of dendritic architecture, along with the stabilization of spines in the peri-infarct region. We found in the same double-treated subjects that the increase in the density of blood vessels was primarily focused in the peri-infarct area. By longitudinally monitoring the calcium functional maps, we found that combined rehabilitation prompted the recovery of essential features of pre-stroke activation profiles, both in spatial and temporal terms. In the same animals presenting large-scale remapping of the injured hemisphere, we observed a significant enhancement of transcallosal functional connectivity after 1 month of rehabilitative therapy. Overall, our study provides an unprecedented view of complementary aspects of cortical anatomical and functional adaptation induced by rehabilitation after stroke.

RESULTS

Experimental Design

We used a photothrombotic model of focal stroke applied to the right M1 of GCaMP6f or GFPM mice (STROKE, TOXIN, ROBOT, and REHAB groups). To restore the interhemispheric balance perturbed by stroke, we performed a focused inactivation of the forelimb motor cortex in the hemisphere contralateral to the ischemic lesion by means of intracortical injections of the synaptic blocker BoNT/E (TOXIN group). BoNT/E is a bacterial enzyme that enters synaptic terminals and reversibly blocks neurotransmission by cleaving synaptosomal-associated protein of 25 kDa (SNAP-25), a main component of the SNARE (soluble NSF-attachment protein receptor) complex (Caleo et al., 2007). We next tested the impact of physical rehabilitation by training the affected forelimb of stroke mice daily with controlled, repeatable, and targeted exercises, guided by a robotic platform—namely, the M-Platform (ROBOT group; Spalletti et al., 2014). Rehabilitation-associated training on the M-Platform consisted of repeated cycles of passively actuated contralesional forelimb extension followed by its active retraction triggered by an acoustic cue (Figure 1A; Video S1). Finally, we tested the synergistic effect of combined therapy. The combined rehabilitation paradigm of the REHAB group consists of a combination of motor training on the M-Platform and pharmacological inactivation of the contralesional hemisphere via BoNT/E (Figure 1B).

ROBOT and REHAB mice were trained for 4 weeks starting 5 days after injury (Figure 1C), in line with the consensus that the initiation of rehabilitative training 5 or more days after stroke is mostly beneficial and has no adverse effects (Krakauer et al., 2012). The motor task was rapidly learned and easily performed. Indeed, the amplitude and slope of the force peaks exerted during the voluntary forelimb-pulling task were not significantly different across groups, neither within a week nor across weeks of training (Figure 1D).

Combined Rehabilitation Preserves Pyramidal Neurons' Architecture and Promotes the Stabilization of Synaptic Contacts in the Peri-infarct Area

In the present study, we assessed how different rehabilitative approaches prompt large- and small-scale cortical plasticity. In particular, we wondered if the improved performance in generalized motor tasks induced exclusively by the combined treatment (Spalletti et al., 2017) resulted in distinct features of cortical reorganization. We investigated synaptic dynamics, vascular network remodeling, and remapping of motor representation.

First, we explored structural rewiring of dendrites and spines. Heightened spontaneous structural remodeling was observed in mice at both presynaptic (axonal fibers and terminals) and postsynaptic (dendrites and dendritic spines) sites in the peri-infarct cortex in the weeks following stroke (Brown et al., 2010; Carmichael et al., 2001; Dancause et al., 2005; Hsu and Jones, 2006; Ueno et al., 2012). In this set of *in vivo* experiments, we performed TPF microscopy of pyramidal apical dendrites and axons (0–100 μm deep from the pial surface) with increasing distances (up to 4 mm) from the stroke core in the cortex of GFPM mice (Figure S1A). The orientations of dendrites and axons were evaluated on the fourth week after performing the lesion (STROKE, TOXIN, ROBOT, and REHAB mice).

A strong orientation gradient of dendrites induced by the collapse of dead tissue in the ischemic core was evident in the STROKE group (Figures 2A, right panels, and 2B). Reorientation was not detectable at distal regions from the ischemic core (>1 mm; Figures S1B and S1C). A strong alignment of neurites in the peri-infarct region was observed in stroke mice treated with BoNT/E (TOXIN group; Figure 2B). Four weeks of robotic training (ROBOT group) were not sufficient to hinder the formation of this structural abnormality. In contrast, reorientation was not visible in REHAB animals, nor in proximal (Figure 2B) or distal (Figure S1C) regions. Indeed, the randomness in dendrite orientation in REHAB mice resembled the one observed in healthy (CTRL) subjects (Figure 2B).

Alterations induced by ischemic damage on neural circuitry are known to affect dendrites as well as synaptic contacts, producing a large increase in spine turnover in the peri-infarct areas of spontaneously recovering mice (Brown et al., 2007; Mostany et al., 2010). We next asked how different rehabilitative approaches modified the synaptic turnover. We thus monitored the appearance and disappearance of apical dendritic spines (Figure 2C) by performing a frame-by-frame comparison of spines in the mosaic we acquired along the rostro-caudal axis with TPF microscopy. We first evaluated the peri-infarct plasticity of pyramidal neurons in spontaneously recovering mice (STROKE) and verified that this focal lesion triggers an increased instability of synaptic contacts. Surprisingly, the single treatments by inhibition of the contralesional hemisphere or physical therapy alone were not able to reinstate physiological levels of spine plasticity (Figure 2D).

On the contrary, spines in the peri-infarct region of REHAB animals exhibited an increased synaptic stability (Figure 2D, left panel) and a lower turnover (Figure 2D, middle panel) than STROKE mice, comparable to healthy CTRL values. The combined rehabilitative treatment also resulted in higher synaptic densities, thereby recapturing an important feature of pre-stroke conditions (Figure 2D, right panel). The stabilization of synaptic contacts induced by rehabilitation was stronger at the proximal level and weakened with increasing distance from the ischemic core (Figure S1D, upper and middle panels). Interestingly, the change in the density of spines extended beyond the peri-infarct region (Figure S1D, lower panel).

In brief, longitudinal imaging of cortical neurons revealed that the combined rehabilitative therapy was necessary to preserve the organization of dendritic arbors in the peri-infarct cortex and to restore dendritic spine plasticity.

Combined Rehabilitative Treatment Stimulates Angiogenesis in the Peri-infarct Area

Since stroke profoundly altered the spatial distribution of superficial blood vessels (Figure 2A, left panels), we wondered if and how rehabilitation altered the vascular milieu in the ipsilesional cortex. To test this, we longitudinally observed mouse cortices of all groups under both cranial window and thinned skull preparations for 1 month after stroke. We found that the injured area progressively shrank, owing to the collapse of dead tissue in STROKE and REHAB mice (Figures 2A, 3A, and S2). In addition, a very bright area appeared in the peri-infarct region of both groups of GCaMP6 mice, possibly representing an excitotoxic response associated with calcium dysregulation (Ankarcrona et al., 1995) elicited by the photothrombotic stroke (13 out of 14 STROKE and REHAB mice; Figure 3A, left panel). The enhanced brightness gradually diminished and disappeared after the acute period (6–19 days after injury in STROKE and REHAB mice; see examples in Figures 3A, right panel, and S2) and was accompanied by a large shrinkage of the necrotic tissue. The consequent displacement of the peri-infarct area was associated with a substantial remodeling of blood vessels (white arrowheads in Figure 3A), in agreement with previous studies (Brown et al., 2007).

We quantified the structural reshaping of cortical vasculature by performing high-resolution 3D reconstructions with TPF microscopy. Specifically, after the last motor training session, we stained the brain vasculature of GFPM mice with a vessel-filling fluorescent dye, albumin-fluorescein isothiocyanate (FITC; Figure 3B). By imaging Thiodiethanol (TDE)-cleared cortical slices (see STAR Methods), we obtained high-resolution 3D maps of blood vessels of the injured, right hemisphere (Figure 3C; Video S2). The reorganization of cortical tissue (Figure 2A) that led to a considerable alignment of dendrites toward the stroke core produced an analogous re-orientation of blood vessels in the peri-infarct area of STROKE mice (Figure 3D). Interestingly, neither the single treatment (TOXIN and ROBOT mice) nor the combined rehabilitation (REHAB) could rescue the random vascular orientation of pre-stroke conditions in the peri-infarct (proximal; <500 μm) region (Figure 3D). A less-pronounced orientation was visible in all groups at distal regions (1000–1500 μm from core; Figure S3A).

Next, we wondered whether rehabilitation triggered angiogenesis in the ipsilesional cortex. We found that the single treatments (TOXIN and ROBOT groups) did not have any significant impact on blood vessel numbers (Figure 3E, left panel). Conversely, the density of blood vessels near the infarct site was significantly higher in REHAB mice compared to both STROKE and CTRL groups.

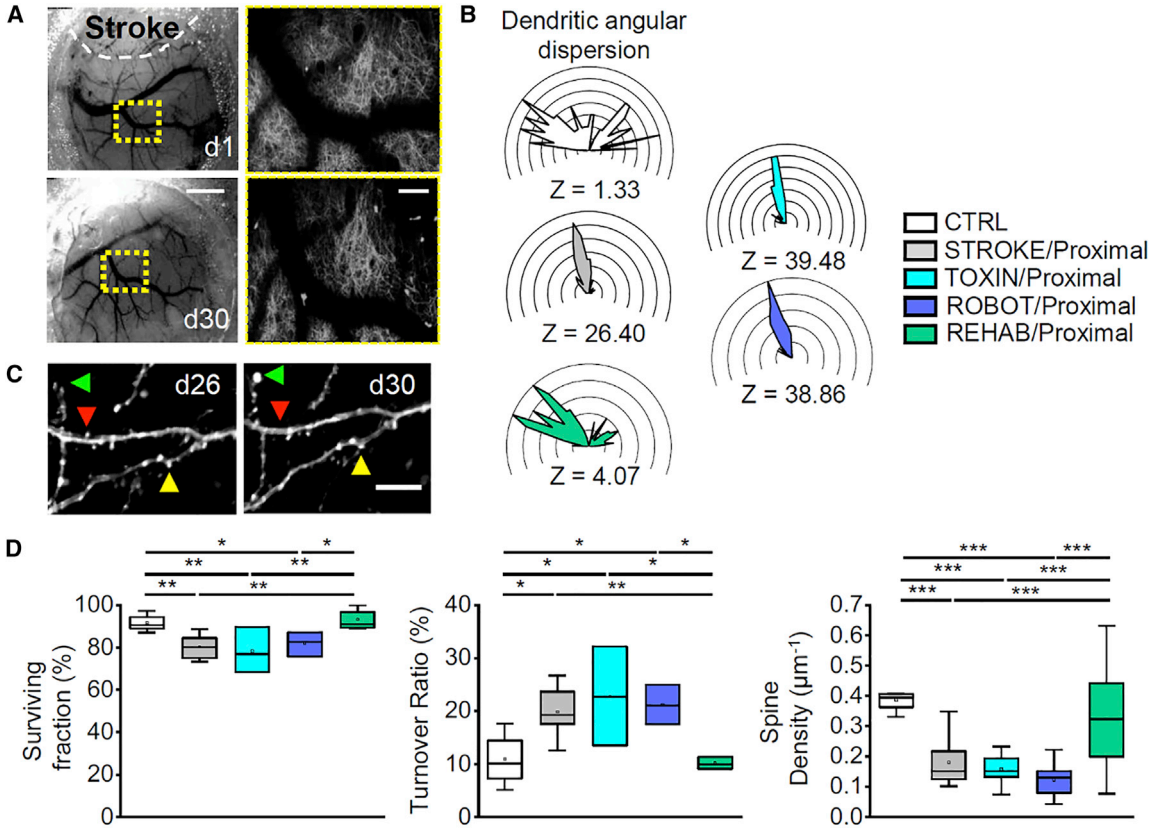

Figure 2. Combined Rehabilitation Affects Dendritic Orientation and Stabilizes Spine Turnover

(A) Brightfield images showing cranial window 1 and 30 days after stroke (STROKE group). The rostral shift of cortical tissue due to the shrinkage of the stroke core is highlighted by the displacement of a reference point (i.e., blood vessel branching point) framed by the dotted yellow square. Scale bar, 1 mm. Panels on the right show the stitched two-photon images (4 × 4 maximum intensity projections [MIPs] of 130 × 130 × 50 μm^3) acquired within the region framed by the respective yellow squares in the left panels. Scale bar, 100 μm.

(B) Polar plots showing angular distribution of dendrites in the peri-infarct area. Plots are oriented as in (A), where lesioned area is toward the uppermost center of the plot (for all panels, n $mice_{CTRL}$ = 5; n $mice_{STROKE}$ = 6, n $mice_{TOXIN}$ = 3, n $mice_{ROBOT}$ = 3, n $mice_{REHAB}$ = 5; n dendrites = 20 per mouse). *Z* scores, calculated by Rayleigh test for circular statistics, are reported for each experimental class at the bottom of the polar plot.

(C) MIPs of two-photon stacks (z depth 8 μm) of dendritic branches 26 and 30 days after stroke (STROKE group). Arrowheads point to newly formed (green), lost (red), and stable (yellow) spines. Scale bar, 5 μm.

(D) Box-and-whiskers plot on spine analysis (n $spines_{CTRL}$ = 493, n $spines_{STROKE}$ = 409, n $spines_{TOXIN}$ = 329, n $spines_{ROBOT}$ = 153, n $spines_{REHAB}$ = 176) showing surviving fraction (SF) (left; SF_{CTRL} = 92% ± 2%, SF_{STROKE} = 80% ± 2%, SF_{TOXIN} = 78% ± 6%, SF_{ROBOT} = 81% ± 3%, SF_{REHAB} = 93% ± 2%; one-way ANOVA with post hoc Fisher test, $P_{CTRL/STROKE}$ = 0.006, $P_{REHAB/STROKE}$ = 0.002, $P_{CTRL/TOXIN}$ = 0.008, $P_{REHAB/TOXIN}$ = 0.003, $P_{CTRL/ROBOT}$ = 0.04, $P_{REHAB/ROBOT}$ = 0.02); turnover ratio (TOR) (middle; TOR_{CTRL} = 11% ± 2%; TOR_{STROKE} = 20% ± 2%; TOR_{TOXIN} = 23% ± 5%; TOR_{ROBOT} = 21% ± 2%; TOR_{REHAB} = 10% ± 3%; one-way ANOVA with post hoc Fisher test, $P_{CTRL/STROKE}$ = 0.02, $P_{REHAB/STROKE}$ = 0.01, $P_{CTRL/TOXIN}$ = 0.01, $P_{REHAB/TOXIN}$ = 0.008, $P_{CTRL/ROBOT}$ = 0.03, $P_{REHAB/ROBOT}$ = 0.02); and spine density (SD) (right; n dendrites = 20 per mouse; spine $density_{CTRL}$ = 0.39 ± 0.01 μm^{-1}; spine $density_{STROKE}$ = 0.18 ± 0.02 μm^{-1}; spine $density_{TOXIN}$ = 0.16 ± 0.01 μm^{-1}; spine $density_{ROBOT}$ = 0.12 ± 0.02 μm^{-1}; spine $density_{REHAB}$ = 0.32 ± 0.05 μm^{-1}; one-way ANOVA with post hoc Bonferroni test, $P_{CTRL/STROKE}$ = 4.1 × 10^{-6}, $P_{REHAB/STROKE}$ = 5.5 × 10^{-4}, $P_{CTRL/TOXIN}$ = 1.0 × 10^{-6}, $P_{REHAB/TOXIN}$ = 1.2 × 10^{-4}, $P_{CTRL/ROBOT}$ = 4.3 × 10^{-6}, $P_{REHAB/ROBOT}$ = 2.6 × 10^{-4}) in the peri-infarct area. Values are average ± SEM.

See also Figure S1.

We further evaluated the vascular density over the entire cortical depth to define layer-specific contributions to the overall increase in blood vessel density. Blood vessel distribution was quite uniform in the CTRL mice. Higher density values were localized mainly to the middle and lower layers of the cortex (300–750 μm deep) in the REHAB group (Figure 3E, middle and right panels). We found that the augmented vascular density was mainly observed in regions near the stroke core (Figure 3E, right panel), whereas distal regions did not show any significant increase (Figure S3B).

We then asked whether the higher density was due to an increase in the average diameter of blood vessels. Our results show that there is no significant difference in the distribution of lumen sizes of cortical blood vessels for the five experimental groups (Figure 3F), ruling out possible influences of vasodilation or vasoconstriction in the evaluation of density. Alternatively, the increased density could be due to the ramification of existing vessels, leading to an enriched complexity of the vascular maps. Nevertheless, the evaluation of the number of branching points showed no significant differences between the

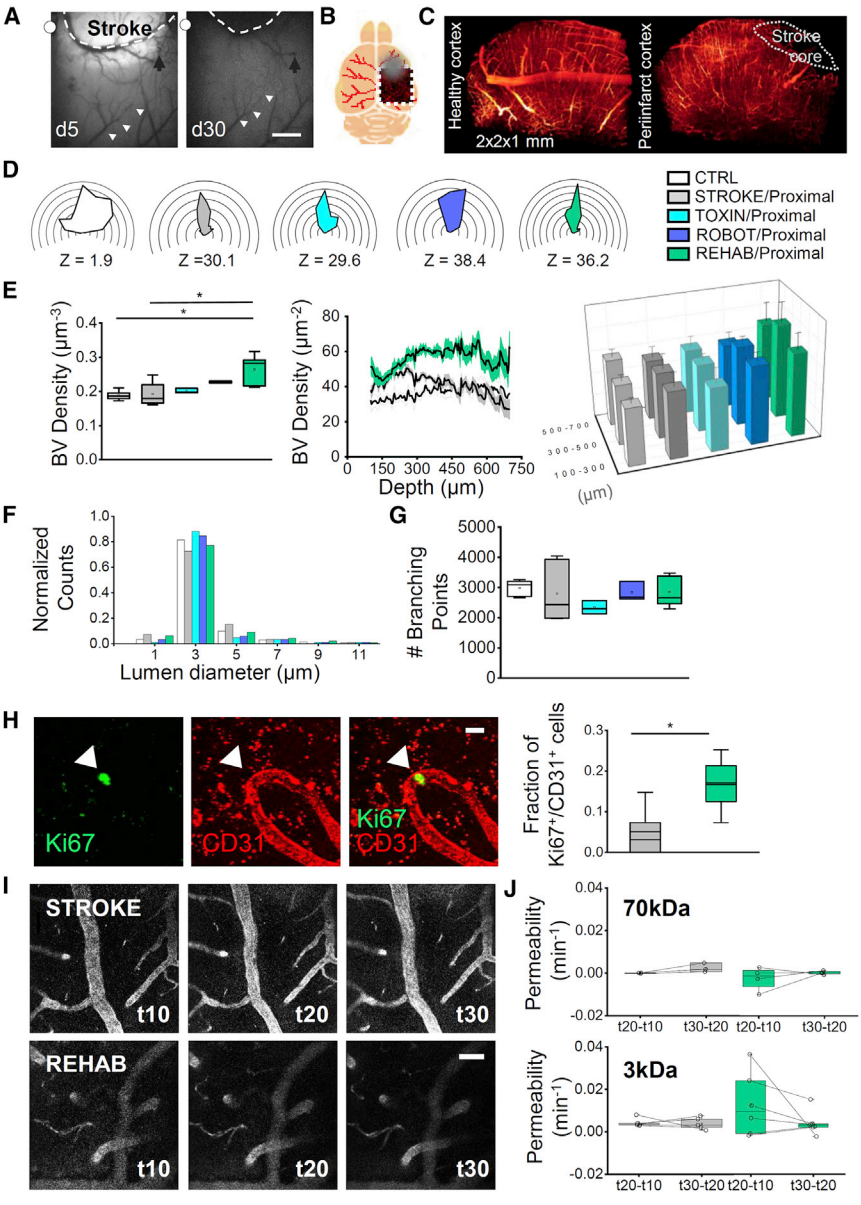

Figure 3. Combined Rehabilitation Promotes Angiogenesis in the Peri-infarct Area

(A) Brightfield images showing cortical vasculature after stroke under a thinned skull preparation. Dotted line emphasizes the profile of a large blood vessel shifting toward the stroke core from 5 to 30 days after stroke; a similar shift is highlighted by the white arrowheads on a blood vessel distal to the injury site. Black arrow points to an internal reference on the image. White dots indicate bregma. Scale bar, 1 mm.

(B) Schematic representation of a fixed brain of a GFPM mouse, in which vasculature is labeled with TRITC (red lines). Dotted square highlights the imaged area; gray circle labels stroke location.

(C) 3D meso-scale reconstruction of vasculature in the healthy contralesional cortex (left) and in the peri-infarct area (right) from TDE-cleared cortical slices. White dotted region highlights the absence of blood vessels in the infarct core.

(D) Polar plots show the distribution of blood vessel orientation in regions proximal to the core for each experimental group measured after the last motor training session (n $mice_{CTRL}$ = 5; n $mice_{STROKE}$ = 6; n $mice_{TOXIN}$ = 3; n $mice_{ROBOT}$ = 3; n $mice_{REHAB}$ = 5; n(blood vessel segments) = 30 per mouse). Plots are oriented as in (A); the lesioned area is toward the uppermost center of the plot. *Z* scores, calculated by the Rayleigh test for circular statistics, are reported for each experimental class below the plot.

(E) Blood vessel (BV) density analysis. (Left) The box-and-whiskers plot shows the blood vessel density in regions proximal to the stroke core in each experimental group (n stacks = 4 per mouse; blood vessel $Density_{CTRL}$ = 0.19 ± 0.01 μm^{-3}; blood vessel $Density_{STROKE\ Proximal}$ = 0.19 ± 0.03 μm^{-3}; blood vessel $Density_{TOXIN\ Proximal}$ = 0.20 ± 0.01 μm^{-3}; blood vessel $Density_{ROBOT\ Proximal}$ = 0.23 ± 0.01 μm^{-3}; blood vessel $Density_{REHAB\ Proximal}$ = 0.26 ± 0.05 μm^{-3}; one-way ANOVA with post hoc Bonferroni test, $P_{REHAB\ Proximal/STROKE\ Proximal}$ = 0.018, $P_{REHAB\ Proximal/CTRL}$ = 0.017). (Middle) Traces indicate blood vessel density with respect to brain cortex depth in each experimental group. Shadows represent SEM. (Right) 3D graph comparing the average blood vessel density (average ± SEM) grouped by cortical depth (100–300 μm from stroke core: blood vessel $Density_{CTRL}$ = 0.18 ± 0.02 μm^{-3}; blood vessel $Density_{STROKE\ Proximal}$ = 0.20 ± 0.04 μm^{-3}; blood vessel $Density_{TOXIN\ Proximal}$ = 0.19 ± 0.05 μm^{-3}; blood vessel $Density_{ROBOT\ Proximal}$ = 0.24 ± 0.03 μm^{-3}; blood vessel $Density_{REHAB\ Proximal}$ = 0.26 ± 0.05 μm^{-3}; 300–500 μm from stroke core: blood vessel $Density_{CTRL}$ = 0.18 ± 0.02 μm^{-3}; blood vessel $Density_{STROKE\ Proximal}$ = 0.20 ± 0.04 μm^{-3}; blood vessel $Density_{TOXIN\ Proximal}$ = 0.21 ± 0.02 μm^{-3}; blood vessel $Density_{ROBOT\ Proximal}$ = 0.24 ± 0.02 μm^{-3}; blood vessel $Density_{REHAB\ Proximal}$ = 0.29 ± 0.06 μm^{-3}; 500–700 μm from stroke core: blood vessel $Density_{CTRL}$ = 0.20 ± 0.02 μm^{-3}; blood vessel $Density_{STROKE\ Proximal}$ = 0.18 ± 0.03 μm^{-3}; blood vessel $Density_{TOXIN\ Proximal}$ = 0.20 ± 0.03 μm^{-3}; blood vessel $Density_{ROBOT\ Proximal}$ = 0.20 ± 0.03 μm^{-3}; blood vessel $Density_{REHAB\ Proximal}$ = 0.24 ± 0.06 μm^{-3}; 300–500 μm from the stroke core: $P_{REHAB\ Proximal/STROKE\ Proximal}$ = 0.024, $P_{REHAB\ Proximal/CTRL}$ = 0.013; one-way ANOVA with post hoc Bonferroni test).

(F) Histogram showing the distribution of lumen diameter of blood vessel for CTRL mice and in the proximal region of STROKE, TOXIN, ROBOT, and REHAB mice (n(blood vessel segments) = 30/animal).

(G) The box-and-whiskers plot shows the quantification of the number of branching points (BPs) in proximal regions (n stacks = 4 per mouse) for each experimental group (number of branching points: BP_{CTRL} = 2979 ± 126; BP_{STROKE} = 2797 ± 390; BP_{TOXIN} = 2332 ± 126; BP_{ROBOT} = 2833 ± 185; BP_{REHAB} = 2852 ± 243).

(H) Immunohistochemical analysis on brain slices (n slices = 7–8 per mouse) with double Ki67 and CD31 labeling. On the left, the images show one example of colocalization of a $Ki67^+$ cell within a $CD31^+$ endothelial cell within a blood vessel in the peri-infarct cortex. The white arrowhead points at the location of the $Ki67^+$ cell in the three panels. On the right, box-and-whiskers plot reports the fraction of double-stained $Ki67^+/CD31^+$ cells in STROKE (n mice = 5) versus REHAB (n mice = 5) mice (fraction of $Ki67^+/CD31^+$cells: STROKE = 0.05 ± 0.03; REHAB = 0.17 ± 0.03; one-tailed p = 0.012). Scale bar, 10 μm.

(I) Representative *in vivo* TPF images of blood vessels acquired 10, 20, and 30 min after injection of fluorescence dextran dye in STROKE (upper row) and REHAB (lower row) mice. Scale bar, 50 μm.

(legend continued on next page)

spontaneously recovering mice (STROKE) and all the treatments (TOXIN, ROBOT, REHAB) or in the proximal (Figure 3G) or distal (Figure S3C) regions, thus ruling out this hypothesis.

Finally, we wondered whether rehabilitation could foster the endothelial proliferation that eventually led to augmented vascular density. We thus compared a group of REHAB mice after 10 sessions of daily robotic training with spontaneously recovering mice (STROKE group) 16 days after stroke. To evaluate endothelial proliferation, we performed *ex vivo* double labeling on brain slices with CD31 and Ki67 (see Supplemental Information). Figure 3H shows that the number of double-stained cells is higher in the peri-infarct region of the cortex of REHAB compared to STROKE mice. The augmented endothelial cell proliferation in combination with the increased density of blood vessels (higher than healthy CTRL mice) and the non-significant change in the lumen diameter in REHAB mice strongly suggests that the combined treatment promotes angiogenesis in the peri-infarct area.

If the newly formed vessels were leaky, this would exacerbate, rather than improve, disease outcomes. To evaluate the permeability of blood vessels, we performed a series of *in vivo* and *ex vivo* measures. We first injected STROKE and REHAB mice with a high-molecular-weight (MW) dye, Texas red dextran, (70 kDa), and evaluated the extravasation over 30 min with TPF microscopy *in vivo* (Figure 3I). We quantified the apparent permeability according to Nhan et al. (2013) by comparing the intra- and extra-vascular fluorescence between two time intervals (10–20 and 20–30 min after injection). Our results show no significant difference in the apparent permeability of cortical blood vessels in the peri-infarct areas of STROKE and REHAB mice 30 days after stroke (Figure 3J, upper panel). To ascertain that the low permeability observed was not dependent on the molecular size, we performed a second set of experiments using the low-MW (3 kDa) fluorescein dextran dye. Low values of permeability were common to both groups (Figure 3J, lower panel). Indeed, no statistically significant difference between STROKE and REHAB mice was observed in any time interval 30 days after stroke. We further wondered if the newly formed blood vessels were leaky at an earlier stage, since they may be not completely mature. The results shown in Figure S3D confirm that the permeability values were comparable between the two groups even 15 days after stroke.

On the perfused brains, we evaluated the diffusion of the dye in the parenchyma over a larger region and across the entire cortex by wide-field fluorescence imaging. We first compared the fluorescence levels between the left and right hemispheres in 3-kDa dye-injected mice 30 days after stroke. The average cortical fluorescence in the ipsilesional cortex was not statistically different across all groups (Figure S3E). In addition, the ratio between the average fluorescence of the peri-infarct and contralesional cortices was comparable in STROKE and REHAB mice (Figure S3F). Finally, the same cortical sections were imaged under a TPF microscope. This measure confirms that there was no significant difference in the fluorescence levels in STROKE versus REHAB mice (Figure S3G). Overall, the combined *in vivo* and *ex vivo* findings indicate that the newly formed vasculature has low permeability, not different from the spontaneously recovered mice.

Taken together, these results on cortical vasculature indicate that the combination of pharmacological and physical therapy triggers substantial blood vessel growth via the promotion of endothelial cell proliferation in the peri-infarct region.

In conclusion, our findings suggest that generalized functional recovery is associated with a pro-angiogenic effect on the vasculature of the peri-infarct area induced by the combined rehabilitative treatment.

Combined Rehabilitation Treatment Restores Cortical Activity Patterns Disrupted by Stroke

We next assessed if combined rehabilitation modulated cortical motor representation activated by voluntary movement of the injured forelimb. We implemented an integrated system for simultaneous imaging of the calcium indicator GCaMP6f over the injured hemisphere and recording of forces applied by the contralesional forelimb during the training sessions on the M-Platform (Figures 4A–4C). Calcium imaging was used as a measure of cortical activity in the brains of GCaMP6f mice. We focused on the analysis of the calcium response activated in the same time window of the voluntary retraction movement (see example in Figure 4C, right panel). The imaging area overlapped with the region visualized on GFPM mice (Figure 4B). Wide-field calcium imaging showed that a small area located in the motor sensory region reproducibly lit up in CTRL mice during the forelimb retraction movement on the M-Platform (examples of cortical activation are reported in Figures 4D and S4A). On the contrary, a large area covering most of the cortical surface of the injured hemisphere was activated while performing the task in non-treated (STROKE) mice 1 month after stroke. Remarkably, calcium activation in REHAB mice was similar to healthy controls (CTRL) in terms of extension, location, timing, and amplitude (Figures 4D–4H and S4A–S4D).

We analyzed the extension and location of the motor representation by overlapping the movement-triggered activation maps obtained on every day of the training week (*ROIg*; see Figures S4B and S4C and STAR Methods). Stroke expanded the motor representation from the M1 toward more caudal regions not specifically associated with motor control (STROKE group in Figure S4C, second panel). Interestingly, the extension of motor representation in REHAB mice was consistently reduced (Figures S4C, third panel, and S4D). In terms of location, the motor

(J) Blood vessel permeability values of STROKE and REHAB mice over two time intervals (10–20 and 20–30 min after injection; 1 stack for each time point) 30 days after stroke. The top panel refers to the permeability to the 70-kDa tracer (n mice$_{STROKE}$ = 3, n mice$_{REHAB}$ = 4; Permeability$_{STROKE}$ (t20–t10) = $-2.0 \times 10^{-5} \pm 1.2 \times 10^{-4}$, Permeability$_{STROKE}$(t30–t20) = 0.002 ± 0.001, Permeability$_{REHAB}$(t20–t10) = −0.002 ± 0.003, Permeability$_{REHAB}$(t30–t20) = $3.1 \times 10^{-4} \pm 4.2 \times 10^{-4}$; one-way ANOVA with post hoc Bonferroni: not significant for all comparisons) and the bottom panel refers to 3-kDa tracer (n mice$_{STROKE}$ = 5, n mice$_{REHAB}$ = 6; Permeability$_{STROKE}$ (t20–t10) = $0.004 \pm 9 \times 10^{-4}$, Permeability$_{STROKE}$(t30–t20) = 0.004 ± 0.001, Permeability$_{REHAB}$(t20–t10) = 0.013 ± 0.006, Permeability$_{REHAB}$(t30–t20) = 0.004 ± 0.002; one-way ANOVA with post hoc Bonferroni: not significant for all comparisons). The values are average ± SEM. See also Figures S2 and S3 and Video S2.

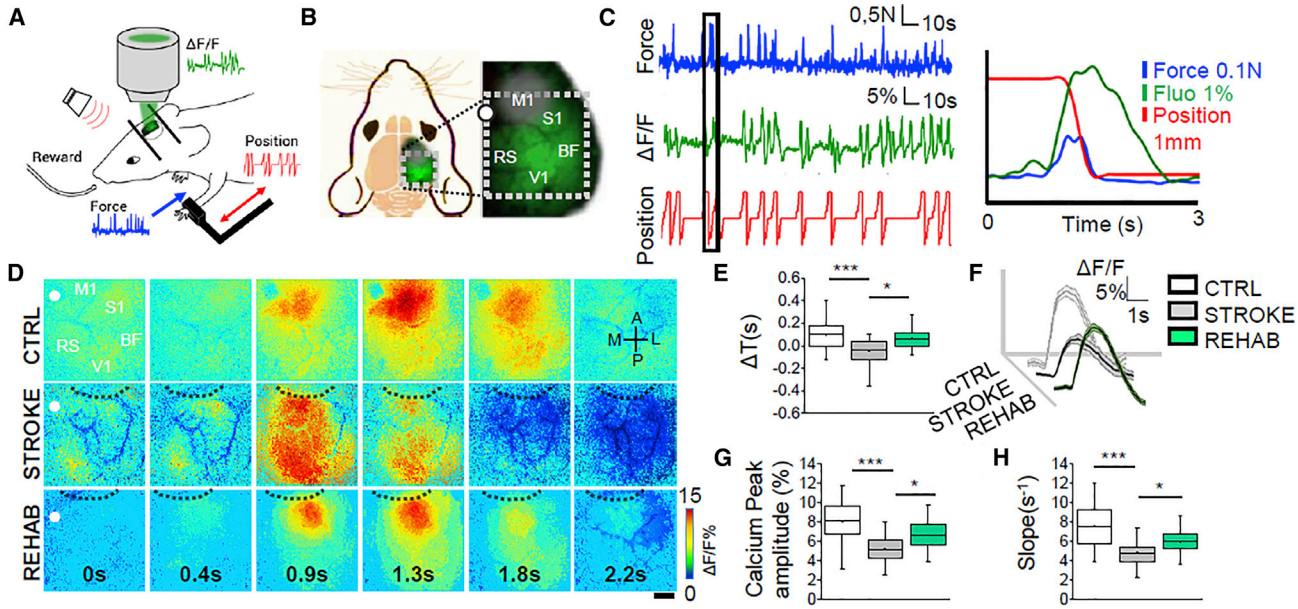

Figure 4. Combined Rehabilitation Counteracts Cortical Dedifferentiation and Restores Activation Profiles in the Post-Stroke, Peri-infarct Region

(A) Schematic representation of M-Platform: examples of simultaneously recorded force (blue), position (red), and ΔF/F traces (green) are reported.

(B) Schematic representation of field of view (i.e., area within the dotted white square) used for wide-field calcium imaging in GCaMP6f mice. The gray circle on the M1 region highlights the location and approximate extent of the lesion. M1, primary motor area; S1, primary somatosensory area; BF, barrel field; V1, primary visual cortex; RS, retrosplenial cortex. White dot indicates the bregma.

(C) Example of force trace (blue), fluorescence trace (green), and handle position (red). The graph on the right shows an overlap of simultaneously recorded traces corresponding to the black box on the left.

(D) Image sequence of cortical activation as assessed by calcium imaging during pulling of the handle by the contralateral forelimb, from 0.4 s before to 1.8 s after the onset of the force peak. Each row shows a representative sequence from a single animal of each group. Black dashed lines define the lesion borders. Scale bar, 1 mm.

(E) Delays in cortical activation in caudal regions in response to contralateral forelimb retraction are shown for the three groups (n $mice_{CTRL}$ = 4, n $transients_{CTRL}$ = 272, n $mice_{STROKE}$ = 6, n $transients_{STROKE}$ = 308, n $mice_{REHAB}$ = 6, n $transients_{REHAB}$ = 343; ΔT_{CTRL} = 0.10 ± 0.03 s, ΔT_{STROKE} = −0.04 ± 0.02 s, ΔT_{REHAB} = 0.06 ± 0.02 s; Kruskal-Wallis one way followed by Tukey's test: $P_{STROKE/CTRL}$ = 0.006, $P_{REHAB/STROKE}$ = 0.016).

(F) Average calcium traces recorded in the region of maximal activation, *ROIg* (see STAR Methods), during contralateral forelimb retraction for the experimental groups; the shadows indicate SEM values.

(G) Graph shows the maximum of fluorescence peaks from the same calcium traces as in (F) (Peak $amplitude_{CTRL}$ = 8.1% ± 0.5%; Peak $amplitude_{STROKE}$ = 5.2% ± 0.3%; Peak $amplitude_{REHAB}$ = 6.6% ± 0.3%; one-way ANOVA followed by Tukey's test: $P_{STROKE/CTRL}$ = 0.000005, $P_{REHAB/STROKE}$ = 0.017).

(H) Graph shows the slope (average ± SEM) of the fluorescence in the rising phase of the trace ($Slope_{CTRL}$ = 7.5 ± 0.5 s^{-1}; $Slope_{STROKE}$ = 4.8 ± 0.2 s^{-1}, $Slope_{REHAB}$ = 6.0 ± 0.2 s^{-1}; Kruskal-Wallis one way followed by Tukey's test: $P_{STROKE/CTRL}$ = 0.00004, $P_{REHAB/STROKE}$ = 0.015). Values are average ± SEM. See also Figure S4.

representation of REHAB mice was centered on the motor-associated region in the peri-infarct area (Figures S4C, third panel, and S4D). The localization and spread of motor maps changed progressively along the weeks of training (Figure S4F). In most cases (5 out of 6 REHAB mice), we found a higher correlation (i.e., augmented functional connectivity) in the activity of spared motor-associated areas (Figure S4E) at the end of the training period (REHAB/4W) compared to the beginning (REHAB/1W). We hypothesized that focalized versus spread motor representations could be associated with different patterns of propagation of calcium activity. To quantify the concurrent recruitment of motor-associated and other functional areas, we analyzed the temporal profile of movement-triggered calcium transients over the injured hemisphere. We assumed that an extended activation (as in STROKE mice) implied a synchronicity in the activation of the rostral peri-infarct and the caudal areas. Indeed, we found that the delay between the maximum calcium peaks of the rostral and caudal regions was slightly negative in STROKE mice, indicating that the activation of the caudal region somewhat preceded the activation of the rostral (peri-infarct) one (Figure 4E). Conversely, the delay was positive in CTRL and REHAB mice. Longitudinal imaging showed that the temporal pattern of rostro-caudal calcium activation in REHAB mice was gradually recovered toward pre-stroke conditions during 4 weeks of training (Figure S4G, left panel).

To sum up, the combined rehabilitative treatment focalized the motor representation to the peri-infarct region. The motor representation of REHAB mice closely resembled that observed in CTRL animals, both spatially and temporally.

We further analyzed calcium transients in the peri-infarct area during contralateral forelimb retraction in CTRL, STROKE, and REHAB mice. At a glance, the average traces in Figure 4F

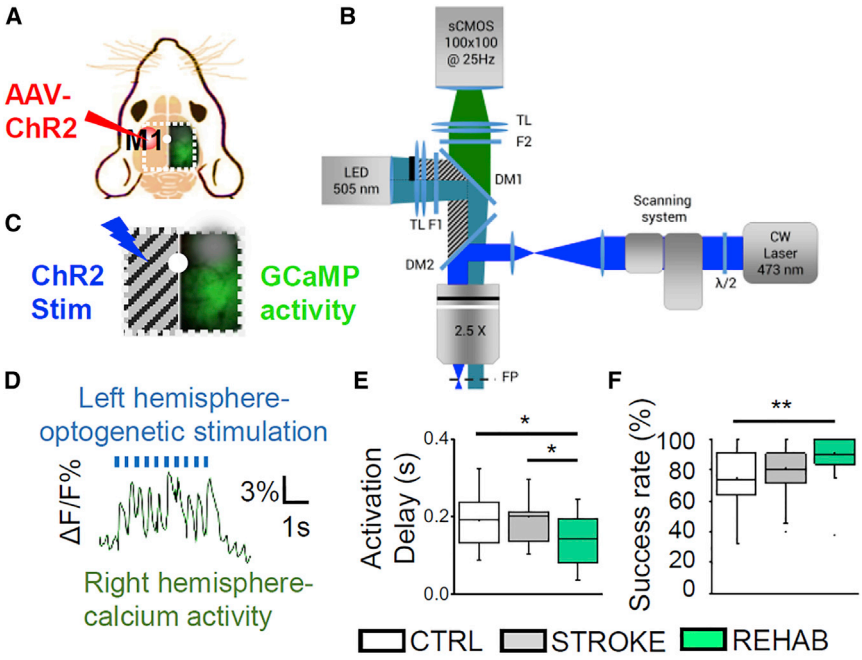

Figure 5. Combined Rehabilitation Strengthens Inter-hemispheric Connectivity after Stroke

(A) Schematic representation of field of view (i.e., area within the white dotted square) for all-optical investigation of inter-hemispheric functional connectivity in GCaMP6f mice. The red circle in the left hemisphere indicates the M1 injected with AAV-ChR2-mCherry. White dot indicates bregma.

(B) Schematic representation of wide-field fluorescence microscope with double illumination path.

(C) Simultaneous ChR2 laser stimulation on the left hemisphere (not illuminated by LED) and detection of the evoked GCaMP6f fluorescence on the right side.

(D) Trace of optogenetically elicited calcium activity in the right cortex.

(E) Box-and-whiskers plot showing the delay between the onset of left hemisphere laser stimulation and the peak of the calcium responses in the right hemisphere (average ± SEM; n $mice_{CTRL}$ = 4, n $stim_{CTRL}$ = 549; n $mice_{STROKE}$ = 3, n $stim_{STROKE}$ = 619; n $mice_{REHAB}$ = 3, n $stim_{REHAB}$ = 654; Activation $Delay_{CTRL}$ = 0.19 ± 0.02 s, Activation $Delay_{STROKE}$ = 0.20 ± 0.02 s, Activation $Delay_{REHAB}$ = 0.14 ± 0.01 s; one-way ANOVA post hoc Fisher, $P < 0.05$ for all comparisons).

(F) Success rate of laser stimulation, calculated as number of times laser stimulation successfully triggered contralateral activation over total number of stimulation trials (average ± SEM, same n mice and n stim as in (E); success $rate_{CTRL}$ = 74 ± 4, success $rate_{STROKE}$ = 81 ± 3, success $rate_{REHAB}$ = 90 ± 3; ANOVA with post hoc Bonferroni test: $P_{REHAB/CTRL} < 0.01$). Values are average ± SEM.

See also Figure S5 and Video S3.

show that stroke (in STROKE mice) and the combined treatment (REHAB mice) modified several features of the calcium transients. While a significant reduction in the amplitude of calcium transients during forelimb retraction was evident 1 month after stroke in the STROKE group, REHAB mice partially recovered to pre-stroke conditions (Figure 4G). In detail, the combined treatment led to a progressive increase in the amplitude of the motor-evoked calcium response over the training period (Figure S4G, middle panel). Moreover, REHAB animals showed a progressively steeper slope of the calcium activation profile along the weeks of training (Figure S4G, right panel). As compared to STROKE animals, a faster rise of the calcium transient in the peri-infarct region was observed in REHAB mice at the end of the training period (Figure 4H). Even though we focused on the analysis of the rise phase of the calcium transient (i.e., slope and amplitude), where the hemodynamic contamination should be very low, we cannot exclude that hemodynamic fluctuations could give a small contribution to the fluorescence signal we recorded in GCaMP6f mice.

In brief, our results show that combined rehabilitative treatment promoted the formation of a new motor representation in the peri-infarct area, where temporal and spatial features of cortical activation recovered toward pre-stroke conditions.

Combined Rehabilitation Improves Inter-hemispheric Functional Connectivity

We hypothesized that the combined treatment alters the functional connectivity of the new motor representation with the contralesional motor cortex. Several studies in mice and humans have shown that interhemispheric M1 connectivity is reduced after stroke (Bauer et al., 2014; van Meer et al., 2010). Therefore, there is growing consensus that increased interhemispheric connectivity positively correlates with the recovery of motor performances in the subacute stage after stroke in humans (Carter et al., 2010). Based on this hypothesis, we tested whether transcallosal projections were altered by combined rehabilitation by using an all-optical approach that combined optogenetic activation of the intact M1 with calcium imaging on the injured hemisphere. In these experiments, the intact (left) M1 of GCaMP6f mice was injected with the adeno-associated virus (AAV9)-CaMKII-ChR2-mCherry to induce the expression of ChR2 in pyramidal neurons (Figure 5A).

One month after stroke, we optogenetically stimulated the intact M1. To avoid ChR2 activation while exciting GCaMP6f fluorescence, we partially occluded the 505-nm light-emitting diode (LED) in our custom-made wide-field microscope (Figures 5B and 5C; see also Conti et al., 2019). Optogenetic stimulation was achieved with a second excitation path in which a 470-nm laser was focused on the AAV-transfected region via acousto-optic deflectors (AODs) (Crocini et al., 2016).

Laser stimulation of the contralesional M1 reproducibly triggered the activation of calcium transients in the injured hemisphere (Figure 5D; Video S3), mainly spreading from the homotopic M1 of CTRL mice, or in the peri-infarct area of STROKE and REHAB animals (Figure S5). Cortical activity then propagated to functionally connected regions that were located either anterior or posterior to the primary source of activation in all three groups of animals (Video S3). By quantifying the delay

between the start of the optogenetic stimulation in the left hemisphere and the peak of calcium activity in the right hemisphere, we found no significant difference between STROKE and CTRL mice (Figure 5E). In contrast, this delay was significantly reduced in REHAB mice, compared to both CTRL and STROKE mice (Figure 5E). In addition, the success rate of contralateral activation in response to optogenetic stimulation was higher in REHAB mice than in CTRL and STROKE animals (Figure 5F). Therefore, this series of all-optical experiments suggests that combined rehabilitation strengthens the functional connectivity between the spared motor cortex and the perilesional cortex 1 month after stroke.

DISCUSSION

In the present study, we showed that rehabilitative treatment combining physical training and BoNT/E inhibition of the contralesional hemisphere stabilized perilesional synaptic contacts, restored features of cortical activation typical of pre-stroke conditions, and promoted the formation of an enriched vascular environment to feed the neuronal population that has been recruited to perform motor control. These results on cortical plasticity induced by rehabilitation *in vivo* provide evidence of the correlation between rehabilitation-induced neuronal and vascular reshaping in the mouse cortex after stroke.

The combined rehabilitation paradigm used here was recently characterized in terms of behavioral assessment of motor recovery (Spalletti et al., 2017). The authors previously developed the M-Platform, a mechatronic device for mouse forelimb training (Spalletti et al., 2014) that mimics a robot for upper limb rehabilitation in humans, the "Arm-Guide" (Reinkensmeyer et al., 2001). The M-Platform was designed with a low level of static friction to allow mice in all conditions (before stroke, right after stroke, and during the weeks under all treatments) to easily perform the motor task from the very first session by applying similar forces. For the same reason, the robotic device is not suitable to evaluate the functional impairment due to stroke. Nonetheless, Spalletti et al. (2017) showed that the M-Platform is an efficient way to assess the recovery of forelimb functionality based on the number of attempts and the time to target, which were progressively reduced over time from the first to the fourth week after stroke. The authors demonstrated that the robotic rehabilitation paradigm per se was not able to generalize recovery to untrained motor tasks (i.e., Schallert Cylinder test). They also showed that even though BoNT/E transiently (day 2 after injection) affected motor functionality of the contralateral forelimb, performance returned to baseline levels on day 9 and remained stable up to 30 days post-injection, as evaluated by behavioral analysis. Importantly, BoNT/E injection into the contralesional motor cortex — silencing synaptic transmission for about 10 days — produced a small and transient improvement in general forelimb motor tests (Gridwalk and Schallert Cylinder test) in stroke mice. Nevertheless, the guide of an appropriate motor rehabilitation regime was necessary to achieve a complete functional recovery. Here, we show that incomplete motor recovery produced by the single treatments is associated with a non-physiological synaptic turnover and reduced spine density. The synergy between the BoNT/E treatment and robotic training, conversely, was able to restore the stability and density of spines of pre-stroke conditions. Finally, our results show that the generalized recovery of motor function exclusively induced by the combined therapy was associated with increased vascular proliferation in the peri-infarct area.

A commonly accepted hypothesis is that the genesis of an enriched vascular milieu around the infarct area might promote synaptogenesis and dendritic remodeling, in addition to axonal sprouting (Brown et al., 2010; Carmichael, 2006; Kelley and Steward, 1997). In parallel, a recent review by Wahl et al. (2014) suggests that rehabilitative training might shape the spared and the new circuits by stabilizing the active contacts. In support of these hypotheses, we show that augmented vascular density induced by the combined rehabilitative treatment is associated with an increased density of synaptic contacts and a stabilization of synaptic turnover. Although there are no other *in vivo* studies examining rehabilitation-induced spine plasticity after stroke to make a direct comparison with, our results are in agreement with recent postmortem histological studies, where rehabilitation was shown to determine significant increases in spine density of distal apical dendrites in corticospinal neurons (Wang et al., 2016).

In this study, we have shown that rehabilitation promotes the recovery of structural features of healthy neuronal networks. Only the combined therapy could rescue the random orientation of pyramidal neurons while supporting the stabilization of synaptic contacts. Interestingly, in the same REHAB mice where stroke profoundly altered the spatial distribution of blood vessels around the core (Figure 3D), the randomness of the dendrite orientation resembled healthy (CTRL) mice (Figure 2B). Further analysis of the acute phase after stroke will allow understanding if random neuronal orientation is maintained or later recovered by rehabilitation.

We hypothesized that the neural plasticity we observed in rehabilitated mice could be supported by revascularization. This assumption is based on the relationship existing between the proangiogenic state and neurological improvement in patients with stroke (Arkuszewski et al., 2009; Hermann and Chopp, 2012; Xiong et al., 2010). The reason could be that the region of active neovascularization acts as a niche for enhanced neuronal remodeling and tissue repair (Prakash and Carmichael, 2015; Shen et al., 2008). Here, we found that vascular density in the peri-infarct area is comparable to healthy animals in stroke non-treated mice (STROKE) and in single treatment groups (TOXIN, ROBOT), while it exceeds physiological values in mice under double treatment (REHAB). Our results suggest that the transient proangiogenic state induced in response to an ischemic insult is enhanced by combined rehabilitation. This hypothesis is supported by our findings on increased endothelial cell proliferation in REHAB mice. In conjunction with the more efficient neuronal activation and stabilized synaptic turnover we measured in the same areas, our study thus suggests that enduring recovery from stroke might result from the association of angiogenesis with neuronal plasticity (Ergul et al., 2012).

We then investigated the changes induced by the combined rehabilitation paradigm on cortical activity. It has been reported that motor-targeted focal stroke induces abnormally scattered cortical maps that persist for months after stroke (see Harrison

et al., 2013). In our study, the diffuse structure of motor representation was observed in non-treated animals (STROKE group). The combined rehabilitation paradigm progressively re-established a cluster of neuronal activity in peri-infarct areas where location, timing, and amplitude parameters highly resembled those of healthy control animals.

Several studies recently addressed the contamination of the blood volume changes on the fluorescence signal of calcium indicators like GCaMP (see, e.g., Ma et al., 2016a, 2016b; Makino et al., 2017; Murphy et al., 2018; Wright et al., 2017). Ma et al. (2016b) showed that the hemodynamic contribution is slower than the GCaMP6f signal, with an average temporal delay of 0.86 ± 0.05 s (representing the phase shift between neural activity and total hemoglobin concentration). More recently, by simultaneously recording (wide-field) calcium dynamics and hemodynamics, Wright et al. (2017) showed that sensory-evoked responses corresponding to oxygenated and deoxygenated hemoglobin have (1) a very slow onset after stimulus presentation, (2) delayed peaks, and (3) low peak magnitudes (see also Murphy et al., 2016) compared to GCaMP6 fluorescence. These studies suggest that the hemodynamic fluctuations, much slower than calcium-associated neuronal activity, affect the late phase of calcium transients more than the rise. Last, by performing wide-field imaging on awake Thy1-GFP mice, Makino et al. (2017) confirmed that the majority of movement-evoked fluorescence changes recorded in Thy1-GCaMP6s mice are due to calcium rather than hemodynamic signals or other artifacts.

By performing optogenetic stimulation on the same group of stroked-afflicted, rehabilitated mice, we demonstrated that the progressive spatial and temporal refocusing of motor control in the ipsilesional cortex is associated with increased interhemispheric connectivity. The functional coupling between homotopic motor cortices was restored 4 weeks after injury in STROKE mice, suggesting that some form of spontaneous recovery compensated for the transcallosal projections lost after stroke. The interhemispheric connectivity is further enhanced after the rehabilitative therapy, suggesting a possible correlation between the recovery of activation patterns in the perilesional area and the reinforcement of connectivity with pyramidal neurons projecting from the healthy M1. While there are no studies examining cortical functionality and transcallosal connectivity (on the same animals) to draw direct comparisons with, our results are consistent with the hypotheses that rehabilitative training of the paretic upper limb can, on the one hand, increase the functional activation of motor regions of the ipsilesional cortex (Hodics et al., 2006; Hubbard et al., 2015) and, on the other, decrease interhemispheric inhibition from the contralesional motor cortex (Harris-Love et al., 2011). We speculate that refocusing of the motor representation could be supported by dendritic rewiring in the peri-lesional area (as shown by our *in vivo* imaging result on structural plasticity), as well as by the activity of contralesional pyramidal cells projecting to the peri-infarct area. Further analysis on targeted neuronal populations is needed to clarify how rehabilitation-induced changes in transcallosal connectivity are specifically linked to alterations in the excitatory-inhibitory balance in the ipsilesional spared tissue.

The mouse stroke model used in this study provides several advantages over more traditional models. Recently, Lim et al. (2014) used voltage-sensitive dyes combined with optogenetics to demonstrate a spontaneous partial recovery of cortical functional connectivity 8 weeks after stroke. The combination of transgenic GCaMP6 mice with AAV-induced expression of ChR2 in the homotopic M1 has the advantage of enabling the reliable control and the stable monitoring of neuronal activity over weeks and months. We anticipate that the all-optical approach we used will be further extended to the longitudinal exploration of the modified transcallosal axonal projections from the injured to the healthy hemisphere in our rehabilitation paradigm.

Our multi-scale investigation brought to light complementary aspects of the structural and functional plasticity induced by rehabilitation that may lead to the development of more efficient therapies and improve post-stroke recovery in patient populations.

STAR★METHODS

Detailed methods are provided in the online version of this paper and include the following:

- KEY RESOURCES TABLE
- LEAD CONTACT AND MATERIALS AVAILABILITY
- EXPERIMENTAL MODEL AND SUBJECT DETAILS
- METHOD DETAILS
  - Photothrombotic Stroke Induction
  - Optical Windows
  - Intracortical Injections
  - Motor Training Protocol on the M-Platform
  - Optogenetic Stimulation and Simultaneous Recording of GCaMP6f Activity
  - Wide-Field Fluorescence Microscopy
  - Two-Photon Fluorescence Microscopy
  - Labeling of Brain Vasculature
- QUANTIFICATION AND STATISTICAL ANALYSIS
- DATA AND CODE AVAILABILITY

SUPPLEMENTAL INFORMATION

Supplemental Information can be found online at https://doi.org/10.1016/j.celrep.2019.08.062.

ACKNOWLEDGMENTS

We thank Alessio Masi and Marie Caroline Muellenbroich for very useful discussions about the manuscript and Giuseppe De Vito for assistance on statistics analysis. We thank Dr. Zanier from the Mario Negri Institute (Milan) for providing reagents for immunohistochemical analysis. We thank the mechanics and electronics workshops at LENS. We thank K. Deisseroth for opsin plasmids. This project has received funding from the H2020 EXCELLENT SCIENCE - European Research Council (ERC) under grant agreement 692943 BrainBIT. In addition, it was supported by the European Union's Horizon 2020 Research and Innovation Programme under Grant Agreements 720270 (HBP SGA1), 785907 (HBP SGA2), and 654148 (Laserlab-Europe). Part of this work was performed within the framework of the Proof of Concept Studies for the ESFRI research infrastructure project Euro-BioImaging at the PCS facility LENS.

AUTHOR CONTRIBUTIONS

A.L.A.M. and M.C. conceived the study. A.L.A.M., E.C., A.P.D.G., C.S., and C.A. performed experiments. S.L., A.L.A.M., E.C., A.S., and A.P.D.G. processed data. A.P., S.L., and L.S. developed the integrated microscope and M-Platform system. F.S.P., S.M., and M.C. obtained funding support. A.L.A.M. and E.C. wrote the paper. All authors approved the paper.

DECLARATION OF INTERESTS

The authors declare no competing interests.

Received: August 2, 2018
Revised: June 19, 2019
Accepted: August 20, 2019
Published: September 24, 2019

REFERENCES

Adkins-Muir, D.L., and Jones, T.A. (2003). Cortical electrical stimulation combined with rehabilitative training: enhanced functional recovery and dendritic plasticity following focal cortical ischemia in rats. Neurol. Res. *25*, 780–788.

Alia, C., Spalletti, C., Lai, S., Panarese, A., Micera, S., and Caleo, M. (2016). Reducing $GABA_A$-mediated inhibition improves forelimb motor function after focal cortical stroke in mice. Sci. Rep. *6*, 37823.

Allegra Mascaro, A.L., Sacconi, L., and Pavone, F.S. (2014). Laser nanosurgery of cerebellar axons in vivo. J. Vis. Exp., e51371.

Ankarcrona, M., Dypbukt, J.M., Bonfoco, E., Zhivotovsky, B., Orrenius, S., Lipton, S.A., and Nicotera, P. (1995). Glutamate-induced neuronal death: a succession of necrosis or apoptosis depending on mitochondrial function. Neuron *15*, 961–973.

Aoyagi, Y., Kawakami, R., Osanai, H., Hibi, T., and Nemoto, T. (2015). A rapid optical clearing protocol using 2,2′-thiodiethanol for microscopic observation of fixed mouse brain. PLoS ONE *10*, e0116280.

Arkuszewski, M., Świat, M., and Opala, G. (2009). Perfusion computed tomography in prediction of functional outcome in patients with acute ischaemic stroke. Nucl. Med. Rev. Cent. East. Eur. *12*, 89–94.

Ayling, O.G., Harrison, T.C., Boyd, J.D., Goroshkov, A., and Murphy, T.H. (2009). Automated light-based mapping of motor cortex by photoactivation of channelrhodopsin-2 transgenic mice. Nat. Methods *6*, 219–224.

Bauer, A.Q., Kraft, A.W., Wright, P.W., Snyder, A.Z., Lee, J.M., and Culver, J.P. (2014). Optical imaging of disrupted functional connectivity following ischemic stroke in mice. Neuroimage *99*, 388–401.

Brown, C.E., Li, P., Boyd, J.D., Delaney, K.R., and Murphy, T.H. (2007). Extensive turnover of dendritic spines and vascular remodeling in cortical tissues recovering from stroke. J. Neurosci. *27*, 4101–4109.

Brown, C.E., Aminoltejari, K., Erb, H., Winship, I.R., and Murphy, T.H. (2009). In vivo voltage-sensitive dye imaging in adult mice reveals that somatosensory maps lost to stroke are replaced over weeks by new structural and functional circuits with prolonged modes of activation within both the peri-infarct zone and distant sites. J. Neurosci. *29*, 1719–1734.

Brown, C.E., Boyd, J.D., and Murphy, T.H. (2010). Longitudinal in vivo imaging reveals balanced and branch-specific remodeling of mature cortical pyramidal dendritic arbors after stroke. J. Cereb. Blood Flow Metab. *30*, 783–791.

Bütefisch, C.M. (2006). Neurobiological bases of rehabilitation. Neurol. Sci. *27* (*Suppl 1*), S18–S23.

Caleo, M., Restani, L., Gianfranceschi, L., Costantin, L., Rossi, C., Rossetto, O., Montecucco, C., and Maffei, L. (2007). Transient synaptic silencing of developing striate cortex has persistent effects on visual function and plasticity. J. Neurosci. *27*, 4530–4540.

Carmichael, S.T. (2006). Cellular and molecular mechanisms of neural repair after stroke: making waves. Ann. Neurol. *59*, 735–742.

Carmichael, S.T., Wei, L., Rovainen, C.M., and Woolsey, T.A. (2001). New patterns of intracortical projections after focal cortical stroke. Neurobiol. Dis. *8*, 910–922.

Carmichael, S.T., Kathirvelu, B., Schweppe, C.A., and Nie, E.H. (2017). Molecular, cellular and functional events in axonal sprouting after stroke. Exp. Neurol. *287*, 384–394.

Carter, A.R., Astafiev, S.V., Lang, C.E., Connor, L.T., Rengachary, J., Strube, M.J., Pope, D.L., Shulman, G.L., and Corbetta, M. (2010). Resting interhemispheric functional magnetic resonance imaging connectivity predicts performance after stroke. Ann. Neurol. *67*, 365–375.

Chen, T.-W., Wardill, T.J., Sun, Y., Pulver, S.R., Renninger, S.L., Baohan, A., Schreiter, E.R., Kerr, R.A., Orger, M.B., Jayaraman, V., et al. (2013). Ultrasensitive fluorescent proteins for imaging neuronal activity. Nature *499*, 295–300.

Clarkson, A.N., Huang, B.S., Macisaac, S.E., Mody, I., and Carmichael, S.T. (2010). Reducing excessive GABA-mediated tonic inhibition promotes functional recovery after stroke. Nature *468*, 305–309.

Conti, E., Allegra Mascaro, A.L., and Pavone, F.S. (2019). Large Scale Double-Path Illumination System with Split Field of View for the All-Optical Study of Inter-and Intra-Hemispheric Functional Connectivity on Mice. Methods Protoc *2*, 11.

Costantini, I., Ghobril, J.P., Di Giovanna, A.P., Allegra Mascaro, A.L., Silvestri, L., Müllenbroich, M.C., Onofri, L., Conti, V., Vanzi, F., Sacconi, L., et al. (2015). A versatile clearing agent for multi-modal brain imaging. Sci. Rep. *5*, 9808.

Crocini, C., Ferrantini, C., Coppini, R., Scardigli, M., Yan, P., Loew, L.M., Smith, G., Cerbai, E., Poggesi, C., Pavone, F.S., and Sacconi, L. (2016). Optogenetics design of mechanistically-based stimulation patterns for cardiac defibrillation. Sci. Rep. *6*, 35628.

Dancause, N., and Nudo, R.J. (2011). Shaping plasticity to enhance recovery after injury. Prog. Brain Res. *192*, 273–295.

Dancause, N., Barbay, S., Frost, S.B., Plautz, E.J., Chen, D., Zoubina, E.V., Stowe, A.M., and Nudo, R.J. (2005). Extensive cortical rewiring after brain injury. J. Neurosci. *25*, 10167–10179.

Di Giovanna, A.P., Tibo, A., Silvestri, L., Müllenbroich, M.C., Costantini, I., Allegra Mascaro, A.L., Sacconi, L., Frasconi, P., and Pavone, F.S. (2018). Whole-Brain Vasculature Reconstruction at the Single Capillary Level. Sci. Rep. *8*, 12573.

Ergul, A., Alhusban, A., and Fagan, S.C. (2012). Angiogenesis: a harmonized target for recovery after stroke. Stroke *43*, 2270–2274.

Fang, P.C., Barbay, S., Plautz, E.J., Hoover, E., Strittmatter, S.M., and Nudo, R.J. (2010). Combination of NEP 1-40 treatment and motor training enhances behavioral recovery after a focal cortical infarct in rats. Stroke *41*, 544–549.

Harris-Love, M.L., Morton, S.M., Perez, M.A., and Cohen, L.G. (2011). Mechanisms of short-term training-induced reaching improvement in severely hemiparetic stroke patients: a TMS study. Neurorehabil. Neural Repair *25*, 398–411.

Harrison, T.C., Silasi, G., Boyd, J.D., and Murphy, T.H. (2013). Displacement of sensory maps and disorganization of motor cortex after targeted stroke in mice. Stroke *44*, 2300–2306.

Hermann, D.M., and Chopp, M. (2012). Promoting brain remodelling and plasticity for stroke recovery: therapeutic promise and potential pitfalls of clinical translation. Lancet Neurol. *11*, 369–380.

Hesse, S., Werner, C., Schonhardt, E.M., Bardeleben, A., Jenrich, W., and Kirker, S.G. (2007). Combined transcranial direct current stimulation and robot-assisted arm training in subacute stroke patients: a pilot study. Restor. Neurol. Neurosci. *25*, 9–15.

Hodics, T., Cohen, L.G., and Cramer, S.C. (2006). Functional imaging of intervention effects in stroke motor rehabilitation. Arch. Phys. Med. Rehabil. *87*, S36–S42.

Holtmaat, A., Bonhoeffer, T., Chow, D.K., Chuckowree, J., De Paola, V., Hofer, S.B., Hübener, M., Keck, T., Knott, G., Lee, W.C., et al. (2009). Long-term, high-resolution imaging in the mouse neocortex through a chronic cranial window. Nat. Protoc. *4*, 1128–1144.

Hsu, J.E., and Jones, T.A. (2006). Contralesional neural plasticity and functional changes in the less-affected forelimb after large and small cortical infarcts in rats. Exp. Neurol. *201*, 479–494.

Hubbard, I.J., Carey, L.M., Budd, T.W., Levi, C., McElduff, P., Hudson, S., Bateman, G., and Parsons, M.W. (2015). A Randomized Controlled Trial of the Effect of Early Upper-Limb Training on Stroke Recovery and Brain Activation. Neurorehabil. Neural Repair *29*, 703–713.

Johnston, D.G., Denizet, M., Mostany, R., and Portera-Cailliau, C. (2013). Chronic in vivo imaging shows no evidence of dendritic plasticity or functional remapping in the contralesional cortex after stroke. Cereb. Cortex *23*, 751–762.

Jones, T.A., and Adkins, D.L. (2015). Motor System Reorganization After Stroke: Stimulating and Training Toward Perfection. Physiology (Bethesda) *30*, 358–370.

Kelley, M.S., and Steward, O. (1997). Injury-induced physiological events that may modulate gene expression in neurons and glia. Rev. Neurosci. *8*, 147–177.

Krakauer, J.W., Carmichael, S.T., Corbett, D., and Wittenberg, G.F. (2012). Getting neurorehabilitation right: what can be learned from animal models? Neurorehabil. Neural Repair *26*, 923–931.

Lee, J.K., Kim, J.E., Sivula, M., and Strittmatter, S.M. (2004). Nogo receptor antagonism promotes stroke recovery by enhancing axonal plasticity. J. Neurosci. *24*, 6209–6217.

Lim, D.H., LeDue, J.M., Mohajerani, M.H., and Murphy, T.H. (2014). Optogenetic mapping after stroke reveals network-wide scaling of functional connections and heterogeneous recovery of the peri-infarct. J. Neurosci. *34*, 16455–16466.

Ma, Y., Shaik, M.A., Kim, S.H., Kozberg, M.G., Thibodeaux, D.N., Zhao, H.T., Yu, H., and Hillman, E.M. (2016a). Wide-field optical mapping of neural activity and brain haemodynamics: considerations and novel approaches. Philos. Trans. R. Soc. Lond. B Biol. Sci. *371*, 20150360.

Ma, Y., Shaik, M.A., Kozberg, M.G., Kim, S.H., Portes, J.P., Timerman, D., and Hillman, E.M. (2016b). Resting-state hemodynamics are spatiotemporally coupled to synchronized and symmetric neural activity in excitatory neurons. Proc. Natl. Acad. Sci. USA *113*, E8463–E8471.

Makino, H., Ren, C., Liu, H., Kim, A.N., Kondapaneni, N., Liu, X., Kuzum, D., and Komiyama, T. (2017). Transformation of Cortex-wide Emergent Properties during Motor Learning. Neuron *94*, 880–890.e888.

Mostany, R., Chowdhury, T.G., Johnston, D.G., Portonovo, S.A., Carmichael, S.T., and Portera-Cailliau, C. (2010). Local hemodynamics dictate long-term dendritic plasticity in peri-infarct cortex. J. Neurosci. *30*, 14116–14126.

Mozaffarian, D., Benjamin, E.J., Go, A.S., Arnett, D.K., Blaha, M.J., Cushman, M., de Ferranti, S., Després, J.P., Fullerton, H.J., Howard, V.J., et al.; American Heart Association Statistics Committee and Stroke Statistics Subcommittee (2015). Heart disease and stroke statistics–2015 update: a report from the American Heart Association. Circulation *131*, e29–e322.

Murphy, T.H., Boyd, J.D., Bolaños, F., Vanni, M.P., Silasi, G., Haupt, D., and LeDue, J.M. (2016). High-throughput automated home-cage mesoscopic functional imaging of mouse cortex. Nat. Commun. *7*, 11611.

Murphy, M.C., Chan, K.C., Kim, S.G., and Vazquez, A.L. (2018). Macroscale variation in resting-state neuronal activity and connectivity assessed by simultaneous calcium imaging, hemodynamic imaging and electrophysiology. Neuroimage *169*, 352–362.

Nhan, T., Burgess, A., Cho, E.E., Stefanovic, B., Lilge, L., and Hynynen, K. (2013). Drug delivery to the brain by focused ultrasound induced blood-brain barrier disruption: quantitative evaluation of enhanced permeability of cerebral vasculature using two-photon microscopy. J. Control. Release *172*, 274–280.

Ollion, J., Cochennec, J., Loll, F., Escudé, C., and Boudier, T. (2013). TANGO: a generic tool for high-throughput 3D image analysis for studying nuclear organization. Bioinformatics *29*, 1840–1841.

Plautz, E.J., Barbay, S., Frost, S.B., Friel, K.M., Dancause, N., Zoubina, E.V., Stowe, A.M., Quaney, B.M., and Nudo, R.J. (2003). Post-infarct cortical plasticity and behavioral recovery using concurrent cortical stimulation and rehabilitative training: a feasibility study in primates. Neurol. Res. *25*, 801–810.

Prakash, R., and Carmichael, S.T. (2015). Blood-brain barrier breakdown and neovascularization processes after stroke and traumatic brain injury. Curr. Opin. Neurol. *28*, 556–564.

Reinkensmeyer, D.J., Takahashi, C.D., Timoszyk, W.K., Reinkensmeyer, A.N., and Kahn, L.E. (2001). Design of robot assistance for arm movement therapy following stroke. Adv. Robot. *14*, 625–637.

Sakadžić, S., Lee, J., Boas, D.A., and Ayata, C. (2015). High-resolution in vivo optical imaging of stroke injury and repair. Brain Res. *1623*, 174–192.

Schneider, C.A., Rasband, W.S., and Eliceiri, K.W. (2012). NIH Image to ImageJ: 25 years of image analysis. Nat. Methods *9*, 671–675.

Shen, Q., Wang, Y., Kokovay, E., Lin, G., Chuang, S.M., Goderie, S.K., Roysam, B., and Temple, S. (2008). Adult SVZ stem cells lie in a vascular niche: a quantitative analysis of niche cell-cell interactions. Cell Stem Cell *3*, 289–300.

Sigler, A., and Murphy, T.H. (2010). In vivo 2-photon imaging of fine structure in the rodent brain: before, during, and after stroke. Stroke *41*, S117–S123.

Spalletti, M., Comanducci, A., Vagaggini, A., Bucciardini, L., Grippo, A., and Amantini, A. (2013). Efficacy of lacosamide on seizures and myoclonus in a patient with epilepsia partialis continua. Epileptic Disord. *15*, 193–196.

Spalletti, C., Lai, S., Mainardi, M., Panarese, A., Ghionzoli, A., Alia, C., Gianfranceschi, L., Chisari, C., Micera, S., and Caleo, M. (2014). A robotic system for quantitative assessment and poststroke training of forelimb retraction in mice. Neurorehabil. Neural Repair *28*, 188–196.

Spalletti, C., Alia, C., Lai, S., Panarese, A., Conti, S., Micera, S., and Caleo, M. (2017). Combining robotic training and inactivation of the healthy hemisphere restores pre-stroke motor patterns in mice. eLife *6*, e28662.

Staudt, T., Lang, M.C., Medda, R., Engelhardt, J., and Hell, S.W. (2007). 2,2′-thiodiethanol: a new water soluble mounting medium for high resolution optical microscopy. Microsc. Res. Tech. *70*, 1–9.

Tennant, K.A., Adkins, D.L., Donlan, N.A., Asay, A.L., Thomas, N., Kleim, J.A., and Jones, T.A. (2011). The organization of the forelimb representation of the C57BL/6 mouse motor cortex as defined by intracortical microstimulation and cytoarchitecture. Cereb. Cortex *21*, 865–876.

Tsai, P.S., Kaufhold, J.P., Blinder, P., Friedman, B., Drew, P.J., Karten, H.J., Lyden, P.D., and Kleinfeld, D. (2009). Correlations of neuronal and microvascular densities in murine cortex revealed by direct counting and colocalization of nuclei and vessels. J. Neurosci. *29*, 14553–14570.

Ueno, Y., Chopp, M., Zhang, L., Buller, B., Liu, Z., Lehman, N.L., Liu, X.S., Zhang, Y., Roberts, C., and Zhang, Z.G. (2012). Axonal outgrowth and dendritic plasticity in the cortical peri-infarct area after experimental stroke. Stroke *43*, 2221–2228.

van Meer, M.P., van der Marel, K., Otte, W.M., Berkelbach van der Sprenkel, J.W., and Dijkhuizen, R.M. (2010). Correspondence between altered functional and structural connectivity in the contralesional sensorimotor cortex after unilateral stroke in rats: a combined resting-state functional MRI and manganese-enhanced MRI study. J. Cereb. Blood Flow Metab. *30*, 1707–1711.

Wahl, A.S., Omlor, W., Rubio, J.C., Chen, J.L., Zheng, H., Schröter, A., Gullo, M., Weinmann, O., Kobayashi, K., Helmchen, F., et al. (2014). Neuronal repair. Asynchronous therapy restores motor control by rewiring of the rat corticospinal tract after stroke. Science *344*, 1250–1255.

Wang, L., Conner, J.M., Nagahara, A.H., and Tuszynski, M.H. (2016). Rehabilitation drives enhancement of neuronal structure in functionally relevant neuronal subsets. Proc. Natl. Acad. Sci. USA *113*, 2750–2755.

Wright, P.W., Brier, L.M., Bauer, A.Q., Baxter, G.A., Kraft, A.W., Reisman, M.D., Bice, A.R., Snyder, A.Z., Lee, J.M., and Culver, J.P. (2017). Functional connectivity structure of cortical calcium dynamics in anesthetized and awake mice. PLoS ONE *12*, e0185759.

Xiong, Y., Mahmood, A., and Chopp, M. (2010). Angiogenesis, neurogenesis and brain recovery of function following injury. Curr. Opin. Investig. Drugs *11*, 298–308.

STAR★METHODS

KEY RESOURCES TABLE

REAGENT or RESOURCE	SOURCE	IDENTIFIER
Antibodies		
CD31	BD PharMingen	Cat# 557355; RRID:AB_396660
Ki67	Abcam	Cat# ab833; RRID:AB_306483
Virus Strains		
AAV9-CaMKIIa-hChR2(H134R)-mCherry	DBA Italia	VB4411
Chemicals, Peptides, and Recombinant Proteins		
Zoletil	Virbac	101580025
Xylazine	Dechra	103595017
Rose Bengal	Sigma	330000
Phosphate Buffer Saline	Sigma	P-4417
Lidocaine 2%	Zoetis Italia srl	100319019
Dexamethasone	MSD	101866034
Paraformaldehyde	Sigma	158127
Botulinum Neurotoxin E	Other	-
Deposited Data		
Wide-field calcium imaging data in combined rehab mice	Mendeley	https://doi.org/10.17632/kt8h855hhc.1
Software for wide-field calcium analysis	GitHub	https://github.com/letiziaallegra/calciumcombinedrehab
Experimental Models: Organisms/Strains		
Mouse: C57BL/6J-Tg(Thy1GCaMP6f)GP5	The Jackson Laboratories	RRID:IMSR_JAX:025393
Mouse: Tg(Thy1-EGFP)MJrs/J	The Jackson Laboratories	RRID:IMSR_JAX:007788
Software and Algorithms		
ImageJ	Schneider et al., 2012	https://imagej.nih.gov/ij/
OriginPro	OriginLab	https://www.originlab.com/

LEAD CONTACT AND MATERIALS AVAILABILITY

Further information and requests for resources and reagents should be directed to and will be fulfilled by the Lead Contact, Anna Letizia Allegra Mascaro (allegra@lens.unifi.it).

This study did not generate new unique reagents.

EXPERIMENTAL MODEL AND SUBJECT DETAILS

All procedures involving mice were performed in accordance with the rules of the Italian Minister of Health, authorization n. 183/2016-PR. Mice were housed in clear plastic cages under a 12 h light/dark cycle and were given *ad libitum* access to water and food. Each group contained comparable numbers of male and female mice, and the age of mice was consistent between the groups (4-12 months). Animals were randomly assigned to experimental groups. We used two different mouse lines from Jackson Laboratories (Bar Harbor, Maine USA): Tg(Thy1-EGFP)MJrs/J (RRID:IMSR_JAX:007788, referred to as GFPM mice) for two-photon imaging experiments and C57BL/6J-Tg(Thy1GCaMP6f)GP5.17Dkim/J (RRID:IMSR_JAX:025393, referred to as GCaMP6f mice) for wide-field and optogenetics. Both lines express a genetically-encoded fluorescent indicator controlled by the Thy1 promoter. We used both heterozygous and positive homozygous mice. A subset of GFPM mice imaged for the structural plasticity experiment (dendrites and spines analysis) were used for blood vessels evaluation; a subset of GCaMP6f mice previously used for calcium imaging were analyzed for inter-hemispheric connectivity.

METHOD DETAILS

Photothrombotic Stroke Induction

All surgical procedures were performed under Zoletil (50 mg/kg) and xylazine (9 mg/kg) anesthesia, unless otherwise stated. After checking by toe pinching that a deep level of sedation was reached, the animals were placed into a stereotaxic apparatus (Stoelting, Wheat Lane, Wood Dale, IL 60191). The skin over the skull was cut and the periosteum was removed with a blade. The primary motor cortex (M1) was identified (stereotaxic coordinates +1,75 lateral, −0.5 rostral from bregma). Five minutes after intraperitoneal injection of Rose Bengal (0.2 ml, 10 mg/ml solution in Phosphate Buffer Saline (PBS); Sigma Aldrich, St. Louis, Missouri, USA), white light from an LED lamp (CL 6000 LED, Carl Zeiss Microscopy, Oberkochen, Germany) was focused with a 20X objective (EC Plan Neofluar NA 0.5, Carl Zeiss Microscopy, Oberkochen, Germany) to illuminate the M1 for 15 min and induce unilateral stroke in the right hemisphere. Afterward, the skin over the skull was sutured and the animals were placed in recovery cages until full recovery. The CTRL animals are not subjected to photothrombosis.

Optical Windows

For the experiments on GCaMP6f mice, we performed a thinned skull preparation on the right hemisphere between bregma and lambda to create an optical window. After applying the local anesthetic lidocaine 2% (20 mg/mL), the skin over the skull and periosteum was removed. The skull over most of the right hemisphere was lightly thinned using a dental drill. A cover glass and an aluminum head- post were attached to the skull using transparent dental cement (Super Bond, C&S). We waited at least 4-5 days after the surgery for the mice to recover before the first imaging session. For the experiments on GFPM mice, we created a square (3x5 mm^2) cranial window centered laterally on the right M1 (+1.75 mm from bregma) and extending rostro-caudally from 1 mm posterior to the bregma to lambda. The protocol we followed for cranial window preparation was slightly modified from Holtmaat et al. (2009) and Allegra Mascaro et al. (2014). Briefly, we administered anesthetized mice a subcutaneous injection of dexamethasone (0.04 mL per 2 mg/ml). The animals were then placed into a stereotaxic apparatus; after applying the local anesthetic lidocaine 2% (20 mg/mL), the skin over the skull was removed. Using a dental drill (Silfradent, Forlì-Cesena Italia), the border of the area of interest was thinned and the central part of the bone was then gently removed. The exposed brain was covered with a circular cover glass; the optical window was sealed to the skull with a mixture of dental cement and acrylic glue. Finally, an aluminum head-post was attached onto the skull using dental cement (Super Bond, C&S, Sun medical Moriyama City, Shiga, Japan). The surgery was followed by the first imaging session under the two-photon microscope. If the cranial windows were opaque on the second imaging session, the windows were removed and cleaned, and imaging was performed immediately afterward. After the last imaging session, all animals were perfused first with 20-30 mL of 0.01 M PBS (pH 7.6) and then with 150 mL of Paraformaldehyde 4% (PFA, Aldrich, St. Louis, Missouri, USA).

Intracortical Injections

We used a dental drill to create a small craniotomy over M1, which was identified by stereotaxic coordinates. Botulinum Neurotoxin E (BoNT/E) injections were performed during the same surgical session of the photothrombotic lesions. We injected 500 nL of BoNT/E (80 nM) divided in 2 separate injections of 250 nL at (i) +0.5 anteroposterior, +1.75 mediolateral and (ii) +0.4 anteroposterior, +1.75 mediolateral at 700 μm cortical depth. For virus injections, we delivered 1 μL of AAV9-CaMKIIa-hChR2(H134R)-mCherry ($2.48*10^{13}$ GC/mL) 700-900 μm under the dura. The skin over the skull was then sutured; the animals were placed in a heated cage (temperature 38°C) until they fully recovered.

Motor Training Protocol on the M-Platform

Mice were allowed to become accustomed to the apparatus before the first imaging session so that they became acquainted with the new environment. The animals were trained by means of the M- Platform, which is a robotic system that allows mice to perform a retraction movement of their left forelimb (Spalletti et al., 2014). Briefly, the M-Platform is composed of a linear actuator, a 6-axis load cell, a precision linear slide with an adjustable friction system and a custom-designed handle that is fastened to the left wrist of the mouse. The handle is screwed onto the load cell, which permits a complete transfer of the forces applied by the animal to the sensor during the training session. Each training session was divided into "trials" that were repeated sequentially and consisted of 5 consecutive steps. First, the linear actuator moved the handle forward and extended the mouse left forelimb by 10 mm (full upper extremity extension). Next, the actuator quickly decoupled from the slide and a tone lasting 0.5 s informed the mouse that it should initiate the task. If the animal was able to overcome the static friction (approximately 0.2 N), it voluntarily pulled the handle back by retracting its forelimb (i.e., forelimb flexion back to the starting position). Upon successful completion of the task, a second tone that lasted 1 s was emitted and the animal was given access to a liquid reward, i.e., 10 μl of sweetened condensed milk, before starting a new cycle.

To detect the movement of the wrist of the animal in the low-light condition of the experiment, an infrared (IR) emitter was placed on the linear slide, and rigidly connected to the load cell and thus to the animal's wrist. Slide displacement was recorded by an IR camera (EXIS WEBCAM #17003, Trust) that was placed perpendicular to the antero-posterior axis of the movement. Position and speed

signals were subsequently extracted from the video recordings and synchronized with the force signals recorded by the load cell (sampling frequency = 100 Hz).

All groups performed at least one week (5 sessions) of daily training, starting 26 days after injury for STROKE and TOXIN mice, 5 days after stroke for ROBOT and REHAB groups and after the surgery for CTRL animals.

Optogenetic Stimulation and Simultaneous Recording of GCaMP6f Activity

After the last training session (i.e., 30 days after stroke and at least 2 weeks after AAV injection for the CTRL group) mice were anesthetized under Zoletil (50 mg/kg) and xylazine (9 mg/kg) and placed into the stereotaxic holder. A small (2x2 mm^2) craniotomy was performed over the injected area. After placing the mouse under the wide field fluorescence microscope, we performed repeated laser (473 nm) stimulation (1-2 Hz, pulse duration 3-5 ms, pulse train duration 5 s, laser power at the focal plane 5 mW) on the left M1, which was localized by mCherry fluorescence. Spurious activation of ChR2 from the green LED (used for GCaMP6f fluorescence excitation) was avoided by blocking half the illumination path with a shutter positioned after the collimator.

Wide-Field Fluorescence Microscopy

The custom-made wide-field imaging setup was equipped with two excitation sources for the simultaneous imaging of GCaMP6f fluorescence and light-stimulation of ChR2. For imaging of GCaMP6f fluorescence, a 505 nm LED (M505L3 Thorlabs, New Jersey, United States) light was deflected by a dichroic filter (DC FF 495-DI02 Semrock, Rochester, New York USA) on the objective (2.5x EC Plan Neofluar, NA 0.085, Carl Zeiss Microscopy, Oberkochen, Germany). A 3D motorized platform (M-229 for xy plane, M-126 for z axis movement; Physik Instrumente, Karlsruhe, Germany) allowed sample displacement. The fluorescence signal was selected by a band pass filter (525/50 Semrock, Rochester, New York USA) and collected on the sensor of a high-speed complementary metal-oxide semiconductor (CMOS) camera (Orca Flash 4.0 Hamamatsu Photonics, NJ, USA).

To perform optogenetic stimulation of ChR2 and simultaneous imaging of GCaMP6 fluorescence, we used the double illumination wide-field system described in Conti et al., 2019. Briefly, a 473 nm continuous wavelength (CW) laser (OBIS 473nm LX 75mW, Coherent, Santa Clara, California, United States) was overlaid on the imaging path using a second dichroic beam splitter (FF484-Fdi01-25x36, Semrock, Rochester, New York USA). The system has a random-access scanning head with two orthogonally-mounted acousto-optical deflectors (DTSXY400, AA Opto-Electronic, Orsay France). A 20X objective (LD Plan Neofluar, 20x/0.4 M27, Carl Zeiss Microscopy, Oberkochen, Germany) was used to demagnify the image onto a 100X100 $pixel^2$ area of the sCMOS camera sensor (OrcaFLASH 4.0, Hamamatsu Photonics, NJ, USA). Images (5.2x5.2mm^2) were acquired at 25 Hz.

Two-Photon Fluorescence Microscopy

The custom made apparatus for two-photon microscopy included a mode-locked Ti: Sapphire laser (Chameleon, Coherent Inc.) that supplied the excitation light. The laser beam was scanned in the xy- plane by a galvo system (VM500, GSI Lumonics). An objective lens (XLUM 20X, NA 0.95, WD 2 mm, Olympus) focused the beam onto the specimen. A closed-loop piezoelectric stage (PIFOC ND72Z2LAQ, PhysikInstrumente, Karlsruhe Germany) allowed axial displacements of the objective up to 2 mm with micrometric precision. Finally, the fluorescence signal was collected by a photomultiplier tube (H7710-13, Hamamatsu Photonics). Custom-made software was developed in LabVIEW 2013 (National Instruments).

Labeling of Brain Vasculature

The vasculature was stained using the protocol described by Tsai et al. (2009), except that we replaced fluorescein (FITC)-conjugated albumin with 0.05% (w/v) tetramethylrhodamine (TRITC)- conjugated albumin (A23016, Thermo Fisher Scientific, Waltham, Massachusetts, USA) in order to avoid spectral overlap between GFP and FITC (Di Giovanna et al., 2018). Under deep anesthesia, mice were transcardially perfused first with 20-30 mL of 0.01 M PBS (pH 7.6) and then with 60 mL of 4% (w/v) paraformaldehyde (PFA) in PBS. This was followed by perfusion with 10 mL of fluorescent gel. After perfusion, a low temperature (ice cold) was maintained to ensure rapid solidification of the gel. After 30 min of cooling, the brain was carefully extracted to avoid damage to pial vessels, and it was incubated overnight in 4% PFA at 4°C. Dissected cortices were cleared with thiodiethanol (166782 TDE, Sigma Aldrich, St. Louis, Missouri, USA) (Aoyagi et al., 2015; Costantini et al., 2015; Staudt et al., 2007), specifically with serial incubation in 30% and 63% TDE/PBS for 1 h and 3 h, respectively, at room temperature. The cleared cortices were flattened using a quartz coverslip #No1 (UQG Optics).

For the evaluation of endothelial proliferation, REHAB mice received 10 sessions of daily robotic training after BoNT/E injection and stroke induction. REHAB and STROKE animals were transcardially perfused first with 20-30 mL of 0.01 M PBS (pH 7.6) and then with 4% (w/v) PFA. Brains were post-fixed in PFA and then cryoprotected with 30% (w/v) sucrose for at least 48 hours. 50 μm-thick coronal sections were obtained using a sliding microtome (Leica, Germany). We performed double fluorescence immunohistochemistry (HIC) staining with CD31/Ki67 (CD31, BD PharMingen, 1:100; Ki67, Abcam, 1:400) to label endothelial cells and verify their proliferation state. We measured the total number of $Ki67^+$ cells in the perilesional area (within 500 μm from the ischemic border), distinguishing those inside blood vessels (labeled by CD31). The results of the analysis are expressed as the fraction of double-labeled cells ($Ki67^+/CD31^+$) over the total number of $Ki67^+$ cells, averaged over the sections (8 sections per animal) for each animal.

Permeability of cortical blood vessels was evaluated by injecting 3 kDa Fluorescein-Dextran (Thermo Fisher scientific, D1830) and/or 70 kDa Texas Red Dextran (Thermo Fisher scientific, D3306) in STROKE and REHAB mice 15 and 30 days after stroke. A thinned

skull or cranial window surgery was done over the peri-infarct cortex on the day of the injection. We performed two-photon imaging (stacks 300x300 μm wide, 0-100 μm deep under the pia) of the labeled vasculature every 5 minutes from right after to 30 minutes after injection. After the last acquisition, the animals were perfused first with 20-30 mL of 0.01 M PBS (pH 7.6) and then with 4% PFA in PBS and the brains were kept overnight in PFA. On the fixed tissue, the fluorescence of the peri-infarct area was evaluated with wide-field fluorescence microscopy. Briefly, we cut the brain with a brain matrix at the peri-infarct level (< 1mm caudal from stroke core) and took an image (exposure time 40ms; 505 nm LED power after the objective 20mW) of the entire coronal section with a 2X objective (Thorlabs). Finally, *ex vivo* TPF imaging (300x300 μm wide) of the peri-infarct cortex on same coronal section was performed.

QUANTIFICATION AND STATISTICAL ANALYSIS

Two-photon imaging: For the structural plasticity analysis of dendrites and spines of pyramidal neurons, we compared stacks in a vertical mosaic acquired in the rostro-caudal direction. During the last week of training (1st and 4th day), we acquired a mosaic of 100 μm thick stacks (113 × 113 μm^2) distanced 200 μm from each other along the rostro-caudal axis starting from the borders of the stroke core. We grouped stacks near (< 500 μm) and far (from 1000 to 1500 μm) from the core, namely proximal and distal regions, respectively. Dendrite orientation was evaluated on 20 dendrites for each mouse (on average) by measuring frame by frame the angle between each structure and the rostro-caudal axis. The stroke core was considered to be at 0°. Z scores were calculated by the Rayleigh Test for circular statistics to evaluate the angular dispersion of dendrites and blood vessels.

For synaptic plasticity analysis, the fluorescence signal of a spine had to be at least 1standard deviation higher than the dendritic shaft fluorescence to be included in the analysis. We quantified the plasticity of dendritic spines using two functions: surviving fraction (SF) and turnover ratio (TOR); the SF describes the fraction of persistent structures:

$$SF(t) = N(t2)/N(t1)$$

where N(t1) is the number of spines present during the first imaging session (26 days after injury for STROKE, TOXIN, ROBOT and REHAB mice), while N(t2) indicates those structures that present 4 days after the first imaging session. The TOR evaluates the fraction of newly appeared in the images and disappeared structures:

$$TOR\ (t1,\ t2) = (Nnew + Ndisappear)/(N(t1) + N\ (t2))$$

where Nnew is the number of structures that are reported for the first time at time t2, Ndisappear is the number of structures that were present at time t1 but which are no longer present at time t2; N (t1) and N (t2) are the total of spines present on t1 and t2, respectively. Unless otherwise stated, data are reported as mean ± SEM.

For vessel orientation analysis, 1 mm deep stacks with 3 μm z-steps (267 μm lateral size) were acquired by TPF microscopy. From these acquisitions throughout the entire cortical depth of the right hemisphere, we extracted maximum intensity projections (MIPs; 300 μm thick) over selected sub-stacks, avoiding meningeal vessels in the superficial 100 μm. Four MIPs of proximal regions (within 500 μm from the stroke core), and four MIPs of distal regions (1-1.5 mm from the core) for each mouse were analyzed. We analyzed blood vessels of all sizes, excluding pial vessels. Polar plots of vessel orientation were obtained by measuring frame by frame the angle between each structure and the rostro-caudal axis (n = 30 vessels for each group). For the vessel density analysis, the stacks were first binarized using automatic thresholding with ImageJ (Schneider et al., 2012). The sum of the pixel count from histograms of the binarized stacks was used as a measure of blood vessel density. Branching points analysis was performed on 3D stacks with the 3D ImageJ suite1 using the workflow for blood vessel segmentation and network analysis developed at the IRB Barcelona (http://adm.irbbarcelona.org/image-j-fiji#TOC-Blood-vessel-segmentation-and-network-analysis). Volumes of 0.53 × 0.53 × 0.60 mm were analyzed for both Proximal and Distal regions for each sample (Ollion et al., 2013).

To evaluate the permeability of blood vessels *in vivo*, we measured the average fluorescence values within a square Region of Interest centered either inside or right outside a blood vessel (diameter: 27 ± 2 μm) and repeated the measure on the same location over 3 time points (10, 20 and 30 minutes after injection). The permeability α(t) was calculated according to the following formula (from Nhan et al., 2013): α(t) = (dIe/dt)/[(Ii(t)/0.55)-(Ie(t)/(Ve/Vi)]. In the *ex vivo* experiment, the fluorescence averaged over an ROI (0.9 mm2) centered in the middle of the right dorsal cortex was used as a measure of the extravasation of the dye. The relative fluorescence between the two hemispheres was further evaluated as the ratio between the average value measured on the left over the right hemisphere. The average fluorescence was evaluated on a single frame of TPF images over a square ROI (50x50 μm).

Wide-field calcium imaging: during each experimental session, the mouse's head was restrained and placed on the M-platform under the wide-field microscope. To avoid head movement artifacts, each frame of the fluorescence stack was offline registered by using two reference points (corresponding to bregma and lambda) that were previously marked on the glass window during the surgery procedure.

For each stack (*FluoSt*) a median time series of GCaMP6f fluorescence signal (*mF*) was extracted, where the value of mF at each *i-th* time point corresponded to the median value computed on all the pixels of the *i-th* frame of *FluoSt*. The *mF* was then oversampled and synchronized to the 100 Hz force and position signals.

The *mF* was used to define a GCaMP6f fluorescence signal baseline F_0, which was identified by the concomitant absence of fluorescence and force signal deflections. $F_0$was selected within a 2.5 ± 0.7 s interval (*I*) of 62 frames where the fluorescence signal was below 1 standard deviation (STD) of the whole *mF* signal and the corresponding force signal showed a value below of 1 STD of the

whole recorded force signal. The fluorescence signal interval was used to reconstruct a 512x512 matrix, i.e., baseline matrix, in which the value of each pixel *B* of the *{m,n}* coordinates of the matrix was computed as follows:

$$B_{\{m,n\}} = \text{median}\left(p_{\{m,n\},j}\right) \text{ with } j = 1, \bullet\bullet\bullet, N_{\{I\}}$$

where $P_{\{m,n\},i}$ is the value of the pixel *p* of the *{m,n}* coordinates at the *j-th* frame of the interval *I* and $N_{\{I\}}$ is the length of Interval *I*. The baseline matrix was then used to normalize all the frames of the fluorescence stack *FluoSt*.

The noise-threshold of 1 STD of the whole recorded force signal was used as a measure of the force peaks exerted by the animal during the retraction task. According to Spalletti et al. (2013), a force peak is defined as force values that transiently exceed the noise-threshold and result in a movement of the linear slide, as detected by variation of the position signal. To maintain consistency in this analysis, peaks of force that did not result in a movement of the slide were not considered.

The onset of each force peak was used as reference time point to select a sequence of 60 frames (2.4 s, where 0.4 s preceded the force peak) from the *FluoSt*. All sequences were visually checked to exclude possible spurious activation (e.g., early activation or no activation) from the analysis. All the selected sequences (*Seqs*) of the animal *An* on day *d* were compiled, defining a *stack of Seqs*, to compute the Summed Intensity Projection for the *An* at *d* (*SIPAn d*). The *SIP* is a matrix of 512x512 pixels, in which the value *P* of the pixel of the *{m, n}* coordinates is computed as follows:

$$p_{\{m,n\}} = \sum_{k=1}^{Ns} p_{\{m,n\},k}$$

where $P_{\{m,n\},K}$ is the value of the pixel p of the *{m, n}* coordinates at the *k-th* frame of *stack of Seqs,* and N_S is the number of frames of the *stack of Seqs*.

The most active area of the *SIPAn d* was then detected by thresholding the *SIPAn d* with a *median* (*SIPAn d*) + *STD* (*SIPAn d*) threshold value. The threshold *SIPAn d* (*th-SIPAn d*) computed for each week of training on the M-Platform (d = 1,…,4 of week W) was superimposed and the common areas, activated at least for 3 daily sessions out of 5 (60%), were labeled as "regions of interest" (ROIs) of the *SIPAn*. We further refined the analysis by dividing the image into two areas, and identifying one anterior ROI [-0.25 - +1.95 mm from bregma (B), AP] and one posterior ROI[+1.95 - + 4.15 mm from B, AP].

We also used the ROIs defined for each individual animal to identify the average ROIs among mice from the same experimental group: *ROIg* with g = "CTRL," "STROKE," "REHAB/1W" and "REHAB/4W" (see Figures S4C and S4F). Thus, the ROIs from animals of the same group were compiled and further thresholded (60%) to define the *ROIg*. On Figure S4, these *ROIg* were superimposed on a functional reference map based on the intracortical microstimulation (ICMS) studies of Tennant et al. (2011) and Alia et al. (2016).

The extent of the *ROIg* was computed as follows:

$$Area_{ROI} = Area_P \bullet X \bullet N_{ROIg}$$

where $Area_p$ corresponds to the area of a single pixel of the image ($7.4*10^{-5}$ mm^2) and N_{ROIg} is the number of pixels composing the *ROIg*. Moreover, the centroid of each *ROIg* was identified and its Euclidean distance from bregma was computed (Figures S4D and S4F).

The ROIs defined for each individual animal were further used to extract the GCaMP6f fluorescence signal corresponding to the activity of those areas. Indeed, from each frame of the FluoS, only pixels belonging to the selected ROI were considered when calculating the representative median value. Thus, a median time series, F_{ROI}, was extracted from the whole FluoS and was representative of the ROI. The fluorescence signal was normalized $((\Delta F_{ROI}/F_0)100\%)$and low-pass filtered to clean the signal from the detected breathing artifacts (Chebyshev filter with cutting frequency = 9 Hz). The previously detected force peaks were then used to select the GCaMP6f fluorescence peaks from the $(\Delta F_{ROI}/F_0)$ signal.

A time window that lasted 4 s, i.e., *wnd*, and was centered at the onset of the force peak, was used to delimit a part of the $(\Delta F_{ROI}/F_0)$ signal, i.e., F_{wnd}, to identify the corresponding fluorescence peak. A fluorescence peak was defined as the part of F_{wnd} that overcame the value of *median+3STD* calculated for the whole signal $(\Delta F_{ROI}/F_0)$.The onset of the peak was detected as:

$$t_{\{peak\ onset\}} = t_{\left\{min\left(\frac{dF_{wnd}}{dt}\right)\right\}}$$

calculated for the $[t_{st}t_{max}]$ time interval, where t_{st} and t_{max} are the time points corresponding to the start of the *wnd* and the maximum of F_{wnd}, respectively.

From the fluorescence and force peaks, different parameters were computed as follows:

- the maximum of the peak (*Peak amplitude*).
- the *Slope* of the peak was defined as follows:

$$Slope_{\{peak\}} = max\left(\frac{dS}{dt}\right)$$

between the $t_{\{s\ peak\ onset\}}$ and ts_{max} where S = *fluo* or *force* signal.

- the time delay between the occurrence of the maximum of the fluorescence (ΔT).

The first movement time point was defined as the first variation of the position signal $((dx/dt) > 0)$ detected along the *wnd* interval.

Optogenetically-induced calcium activity: On every stack, we analyzed the calcium activity averaged over a round ROI (2.3 mm of diameter) centered on the peri-infarct area. Changing in the variation of fluorescence signal (ΔF/F) triggered by light irradiation of the contralateral hemisphere that were below 1% were excluded from the analysis. A calcium response was considered optogenetically-triggered if it started within 120 ms of optogenetic stimulation. The activation delay refers to the average (±Standard Error of the Mean, SEM) delay of the calcium peak with respect to the onset of laser stimulation. The success rate reports the number of times the laser stimulation successfully triggered contralateral activation over the total number of stimulation trials.

DATA AND CODE AVAILABILITY

Source data for two-photon imaging of spines and dendrites in Figures 2 and S1 in the paper is available upon request. Source data for vasculature imaging in Figures 3 and S3 in the paper is available upon request. Source data for wide-field fluorescence imaging in Figures 4 and S4 in the paper is available on Mendeley (https://data.mendeley.com/datasets/kt8h855hhc/1). Source data for all-optical interrogation of effective connectivity in Figures 5 and S5 in the paper is available upon request. The code for wide-field calcium analysis generated during this study are available at GitHub [https://github.com/letiziaallegra/calciumcombinedrehab].